



# Capacity Design of Coupled Composite Plate Shear Wall–Concrete-Filled System

Morgan Broberg, S.M.ASCE<sup>1</sup>; Soheil Shafaei, M.ASCE<sup>2</sup>; Emre Kizilarslan, S.M.ASCE<sup>3</sup>; Jungil Seo<sup>4</sup>; Amit H. Varma, M.ASCE<sup>5</sup>; Michel Bruneau, F.ASCE<sup>6</sup>; and Ron Klemencic, P.E., S.E., Dist.M.ASCE<sup>7</sup>

**Abstract:** Composite plate shear walls–concrete-filled (C-PSW/CF) are a new and innovative lateral force–resisting system intended for high-rise buildings. High-rise building applications of this system are particularly efficient in the coupled wall configuration, in which the walls are C-PSW/CF and the coupling beams are concrete filled steel box sections. This paper presents a capacity design principle for the seismic design of coupled composite plate shear wall–concrete filled (CC-PSW/CF) systems. The capacity design principle implements a strong wall–weak coupling beam approach, in which flexural yielding occurs in the coupling beams before flexural yielding at the base of walls. The coupling beams are sized to resist the calculated seismic lateral force level. The composite walls are sized to resist an amplified seismic lateral force corresponding to the overall plastic mechanism for the structure, while accounting for the capacity-limited forces from the coupling beams and the coupling action between the walls. The paper summarizes the recommendations and requirements for appropriate sizing of the composite coupling beams and walls. These recommendations were used along with the capacity design principle to design four example (8–22-story) structures and evaluate their seismic behavior. The structures were modeled using benchmarked finite-element models and fiber-based models that accounted for the various limit states, including steel yielding, local buckling, fracture, concrete crushing, confinement, and tension cracking. The numerical models were analyzed for monotonic pushover loading and scaled seismic ground motions. The structural responses from the nonlinear pushover analysis and the nonlinear time history analyses were in accordance with the capacity limited design philosophy, thus confirming its efficacy. DOI: [10.1061/\(ASCE\)ST.1943-541X.0003296](https://doi.org/10.1061/(ASCE)ST.1943-541X.0003296). © 2022 American Society of Civil Engineers.

**Author keywords:** Composite; Steel; Concrete; Seismic; Earthquake engineering; Analysis; Design.

## Introduction

Tall buildings commonly are designed and constructed with reinforced concrete (RC) core walls, steel gravity framing, and light-weight composite steel deck floor systems. The schedule critical aspect of this operation is the construction of RC core walls, which

progresses at a much slower pace than the rest of the structure. With the rise of modularity and prefabricated solutions, industry innovators began looking for solutions to expedite the construction schedule and improve overall project economy. Composite plate shear walls–concrete filled (C-PSW/CF) are a viable alternative to RC core walls (Morgen et al. 2018) because the construction schedule can be expedited by the elimination of formwork (placement and removal), rebar cages (assembly and installation), and falsework (installation and removal). C-PSW/CF also offer opportunities to leverage modularization, prefabrication of steel modules, and optimize concrete casting and curing using self-consolidating concrete. Construction and erection tolerance issues between the steel gravity framing and the C-PSW/CF core system can be minimized by coordination of assembly and erection activities. Despite their innovation and novelty, C-PSW/CF systems rely on standard composite construction techniques already used in practice, reducing the need for extensive worker training.

C-PSW/CF can be used as uncoupled shear walls or as coupled core wall systems. Coupled systems consist of two major types of structural components: C-PSW/CF walls and composite coupling beams. C-PSW/CF walls consist of two exterior steel faceplates that are connected to each other with steel tie bars. Steel-headed stud anchors also may be provided on the interior surfaces of the steel faceplates. These steel modules are prefabricated in the shop, transported to the field, assembled, and then filled with plain concrete. No additional steel reinforcing bars are needed, thus eliminating the need for assembly and placement of rebar cages. The steel modules serve as stay-in-place formwork for concrete placement and also can be designed to serve as the falsework for construction loads, thus eliminating the need for assembly and removal of formwork and falseworks. The composite coupling beams are concrete-filled steel box sections, which also are referred

<sup>1</sup>Graduate Research Assistant, Lyles School of Civil Engineering, Purdue Univ., 1040 S. River Rd., West Lafayette, IN 47907 (corresponding author). ORCID: <https://orcid.org/0000-0003-2406-8117>. Email: [mbroberg@purdue.edu](mailto:mbroberg@purdue.edu)

<sup>2</sup>Postdoctoral Research Assistant, Lyles School of Civil Engineering, Purdue Univ., 1040 S. River Rd., West Lafayette, IN 47907. ORCID: <https://orcid.org/0000-0003-3475-8525>. Email: [sshafaei@purdue.edu](mailto:sshafaei@purdue.edu)

<sup>3</sup>Graduate Research Assistant, Dept. of Civil Structural and Environmental Engineering, Univ. at Buffalo, 212 Ketter Hall, Buffalo, NY 14260. Email: [emrekizi@buffalo.edu](mailto:emrekizi@buffalo.edu)

<sup>4</sup>Research Assistant Professor, Lyles School of Civil Engineering, Purdue Univ., 1040 S. River Rd., West Lafayette, IN 47907. ORCID: <https://orcid.org/0000-0003-0861-4261>. Email: [seo2@purdue.edu](mailto:seo2@purdue.edu)

<sup>5</sup>Karl H. Kettelhut Professor, Lyles School of Civil Engineering, Purdue Univ., 1040 S. River Rd., West Lafayette, IN 47907. ORCID: <https://orcid.org/0000-0001-7153-4681>. Email: [ahvarma@purdue.edu](mailto:ahvarma@purdue.edu)

<sup>6</sup>SUNY Distinguished Professor, Dept. of Civil, Structural, and Environmental Engineering, Univ. at Buffalo, 212 Ketter Hall, Buffalo, NY 14260. ORCID: <https://orcid.org/0000-0003-1170-468X>. Email: [bruneau@buffalo.edu](mailto:bruneau@buffalo.edu)

<sup>7</sup>Chairman and CEO, Magnusson Klemencic Associates, Magnusson Klemencic Associates, 1301 Fifth Ave., Suite 3200, Seattle, WA 98101. Email: [rklemencic@mka.com](mailto:rklemencic@mka.com)

Note. This manuscript was submitted on July 15, 2021; approved on November 9, 2021; published online on February 7, 2022. Discussion period open until July 7, 2022; separate discussions must be submitted for individual papers. This paper is part of the *Journal of Structural Engineering*, © ASCE, ISSN 0733-9445.

to as concrete-filled steel tubes (CFSTs) in the literature. A more extensive review of the system is given in AISC Design Guide 37 (Varma et al. 2022).

Construction of the first building using the coupled C-PSW/CF (or CC-PSW/CF) system in seismic regions topped out in August 2020. The Rainer Square Tower (About Rainier Square, n.d.) stands 58 stories tall in downtown Seattle. This structure was constructed in 10 months, about 40% faster than expected for a RC core building (Post 2020). Over 500 steel modules were prefabricated off-site, transported to the site, erected, and filled with concrete. This structure offers a well-documented proof-of-concept for future CC-PSW/CF buildings and proven construction schedule reduction to incentivize widespread adoption of the system. Construction of the first building using the CC-PSW/CF system in a high seismic region is ongoing in San Jose, California. The 200 Park Avenue building (Home, n.d.) stands 19 stories tall with a total of 89,692 m<sup>2</sup> (965,342 ft<sup>2</sup>) of residential area.

The development of a robust design methodology and detailing requirements will enable designers to implement this CC-PSW/CF system efficiently without having to perform computationally expensive analyses to demonstrate system-level behavior. For consistency with other steel lateral load-resisting systems, and to ensure satisfactory seismic performance, such a robust design methodology must be anchored in capacity design principles. The capacity design concept was developed initially in New Zealand by Park and Paulay (1975). In this design approach, primary energy-dissipating elements of a given structural system are selected and detailed for ductility, whereas other structural elements are designed (per capacity design principles) with sufficient strength to ensure that the target energy dissipating mechanism can be achieved.

## Background

Implementation of capacity-design principles for steel design in North America goes as far back as the 1980 edition of the SEAOC seismic design provisions (SEAOC 1980), which were adopted in the 1985 edition of the Uniform Building Code (ICBO 1985). These provisions required beam-to-column connections in moment-resisting frames to be capable of developing the expected strengths of the beam hinges, and connections of braces in braced frames to be capable of developing the expected strengths of the bracing members. Uang and Bruneau (2018) provided a historical perspective on how this design approach evolved over the last decades into the complete system-based capacity design approach that is at the core of the AISC Seismic Provisions for Steel Buildings, AISC 341-16 (AISC 2016a).

Capacity design principles already have been established for uncoupled C-PSW/CF walls (Alzeni and Bruneau 2017; Kurt et al. 2016). Tests of walls with boundary elements by Alzeni and Bruneau (2017) indicated that the plastic moment capacity ( $M_p$ ) can be estimated conservatively using a plastic stress distribution model for walls with boundary elements. For walls with semicircular boundary elements, Alzeni and Bruneau found the ultimate capacity to be  $1.1M_p$ , whereas for walls with circular boundary elements, the ultimate capacity was  $1.2M_p$  considering the measured material properties and concrete strength. These results suggest that if wall elements are limiting forces for other components, the expected plastic moment capacity ( $M_{p,exp}$ ) of the section may need to consider an amplification factor to capture this additional strength.

Kurt et al. (2016) showed that the capacity of walls without boundary elements (flange plates) can be approximated reasonably as the plastic moment of the section for wall aspect ratios ( $h/l_w$ ) greater than or equal to 1.5. This analysis is supported by

experimental testing and numerical modeling approaches. The plastic moment is calculated using standard plastic stress distribution methods as described in Section I2 of AISC 360-22 (AISC 2016b). The in-plane shear strength of C-PSW/CF walls was evaluated experimentally and numerically by Varma et al. (2011), Seo et al. (2016), and Booth et al. (2020). Equations for conservatively estimating the in-plane shear strength of C-PSW/CF walls were developed based on those studies and included in AISC N690-18 (AISC 2018) and AISC 360-22 (AISC 2022b).

In addition to considering strength approaches, limits on the ductility of the energy-dissipating components also are important in capacity design (Bruneau et al. 2011). For example, in AISC 341-16 (AISC 2016a), moment frames are categorized largely based on the rotation capacity of their beams. No rotational capacity criteria are applied to ordinary moment frame systems, whereas intermediate and special moment frame beams are required to demonstrate rotational capacities of 0.02 and 0.04 rad, respectively, while maintaining a load of at least 80% of their maximum flexural strength. ASCE 7 (ASCE 2022) applies different seismic response coefficients depending on the classification of the system (ordinary, intermediate, or special moment frames).

The superior seismic performance of CC-PSW/CFs over uncoupled walls was demonstrated in a set of FEMA P695 studies performed by Agrawal et al. (2020) on uncoupled systems and by Kizilarlan et al. (2021b) on coupled systems. Those studies employed capacity design principles to size the walls and coupling beams, as applicable. Agrawal et al. (2020) confirmed that a seismic force reduction factor (R factor) of 6.5 was appropriate for uncoupled C-PSW/CF systems, whereas Kizilarlan et al. (2021b) confirmed that an R factor of 8 was appropriate for CC-PSW/CF systems. These values subsequently were implemented in FEMA P-2082-1 (FEMA 2020) and ASCE 7 (ASCE 2022). This R factor of 8 is consistent with recent recommendations for coupled concrete shear walls (Tauberg et al. 2019). The coupled wall study enforced strong wall-weak coupling beam principles to spread plasticity along the height of the structure. In the uncoupled wall study, yielding was limited to the base of wall elements (Agrawal et al. 2020), whereas in the coupled study, yielding occurred in coupling beams before initiation of yielding in the walls (Kizilarlan et al. 2021b).

Much like moment frame systems, this additional ductility is associated with the rotational capacity of the coupling beam elements. Coupling beams designed for the FEMA P695 study included provisions that coupling beams must be flexure-critical (i.e., have a span-to-depth ratio of at least 2.5) and the rotational capacity of coupling beams must be 0.030 rad to use the higher R factor of 8 (Kizilarlan et al. 2021b). Flexure-critical coupling beams connected with complete joint penetration welds to the steel plates of C-PSW/CF have been able to develop this rotation capacity while retaining 80% of their flexural strength (Nie et al. 2014; Varma et al. 2021). Shear-critical coupling beams are not recommended because their ductility and rotation capacity are limited by the shear (compression strut) failure of the cracked concrete between the ends of coupling beams (Nie et al. 2014). This paper details the capacity design principles developed by the authors for the design of CC-PSW/CF and demonstrates through numerical modeling that the desired capacity design limits are implemented successfully for CC-PSW/CF walls when applying these provisions.

## Basis of Design

CC-PSW/CF systems use coupled walls to resist lateral loads such as design basis and maximum considered earthquakes (MCEs).

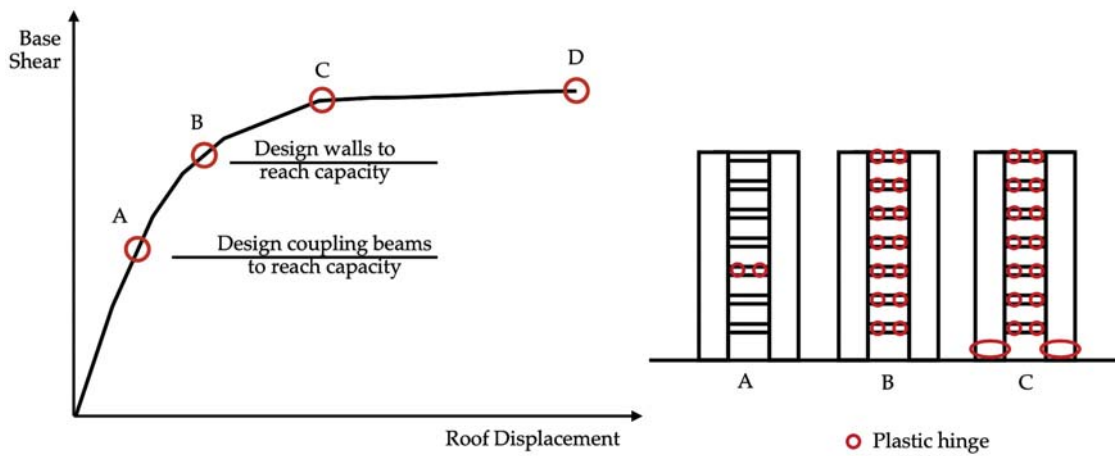


Fig. 1. Desired pushover behavior of the CC-PSW system.

In these events, the coupled wall system is expected to undergo significant inelastic deformation.

Individual C-PSW/CFs have a plastic rotation capacity of 0.015–0.02 rad (Shafaei et al. 2021b). This rotation capacity is concentrated at the base of the C-PSW/CF walls, whereas most of the wall remains essentially elastic along its height. As indicated previously, a seismic response modification factor (R factor) of 6.5 is assigned by ASCE-7 to this uncoupled system. To achieve a higher R factor of 8, the (coupled) CC-PSW/CF system must have better inelastic behavior and dissipate more hysteretic energy than uncoupled C-PSW/CFs. This additional energy dissipation is achieved by plastic hinging of coupling beams in all stories along the height of the building, thereby altering the structure's governing plastic collapse mechanism.

To ensure that the plasticity spreads along the height of the structure and that hinges form in the coupling beams, the system must be proportioned such that the coupling beams yield before yielding in the wall. This progression of failure is required so that the coupling beams engage and dissipate energy—otherwise, as in the uncoupled system, flexural hinging may be limited to the base of the wall and no additional ductility and energy dissipation will be harnessed. In the context of CC-PSW/CF, the coupling beams are concrete-filled box sections. Limited testing of these composite coupling beam-to-wall connections (Nie et al. 2014) suggested that the beam rotation capacity in flexural hinging is greater than the rotation capacity associated with shear yielding. Additionally, concerns about the effects of shear yielding coupling beams on wall behavior, for example, the spread of shear yielding into the wall elements, have not been investigated. Therefore, the system is required to be proportioned with flexure-controlled coupling beams.

The inelastic deformation in CC-PSW/CF systems has two sources: (1) flexural plastic hinges at the ends of coupling beams, and (2) flexural yielding at the base of the walls. As mentioned previously, the preferred inelastic mechanism is to develop plastic hinges at the ends of coupling beams before the developing them at the base of the walls. To achieve this inelastic mechanism the members must be proportioned following a strong wall–weak coupling beam design philosophy. To ensure this type of behavior, a capacity design principle is used. This principle ensures that the loading level associated with the plastic capacity of the wall sections exceeds the loading level associated with the initiation of yielding in the coupling beams. By following the design approached discussed subsequently, the aforementioned objectives will be attained.

## Capacity Design

A capacity design approach was adopted as the design basis. This design approach is used to define the required strengths for components based on the expected strength of fuse elements. In this case, the plastic hinges at the ends of the coupling beams are the designated fuses. The expected strengths of these components are used to define the demand loading (required strengths) for the walls. In other words, the walls are sized to have the capacity to resist the forces imparted to them, including those imparted by all the coupling beams along the height of the structure that have formed flexural plastic hinges at their ends.

Implementing this principle should lead to the characteristic pushover behavior in Fig. 1, in which the initial branch represents elastic behavior with a slope corresponding to the effective stiffness. As the lateral load (and base shear) increases, the load level reaches Point A, corresponding to the equivalent lateral force (ELF) level. This point corresponds to the required strengths (design demands) for the coupling beams, and thus initiation of plasticity in the coupling beams. As the lateral load (and base shear) is increased, the response reaches Point B, at which all coupling beams have formed plastic hinges at both ends. This load level corresponds to the required strengths (design demands) for the walls, and thus potential initiation of plasticity at the base of the walls. As the lateral load is increased, the response reaches the next milestone, Point C, corresponding to the formation of plastic hinges at the base of the walls, and thus formation of the overall inelastic mechanism. Finally, Point D represents fracture failure of the coupling beams or walls in a monotonic pushover behavior.

To implement this design process, a linear elastic frame model is constructed and subjected to ELF level loads. This elastic model accounts for effective axial and flexure stiffness values for both wall and coupling beam elements. Coupling beam effective axial  $[(EA)_{eff}]$  and effective flexural  $[(EI)_{eff}]$  stiffness are calculated per AISC 360-22 (AISC 2016b), Section II.5. C-PSW/CF wall effective stiffnesses can be estimated as the secant stiffness corresponding to 60% of the plastic moment. Alternatively, these stiffness values can be estimated using Eqs. (1)–(3) in AISC 360-22 (AISC 2022b) Section II.6, which were developed by Agrawal et al. (2020) by calibrating linear elastic models to nonlinear models (with concrete cracking) subjected to ELF level loads. These stiffness values also were shown to match closely the stiffness values calculated using the secant stiffness corresponding to 60% of the plastic moment

$$(EI)_{\text{eff}} = E_s I_s + 0.35 E_c I_c \quad (1)$$

$$(EA)_{\text{eff}} = E_s A_s + 0.45 E_c A_c \quad (2)$$

$$(GA)_{\text{eff}} = E_s A_s + E_c A_c \quad (3)$$

This elastic model is used to calculate the required strengths (or design demands) for coupling beams and the story drifts for the structure. These calculated story drifts are compared with the corresponding drift limits specified by the applicable building code. After designing the coupling beam sections to provide available (design) strength greater than or equal to the required strength, the walls are designed as capacity-protected members. At the core of this analysis is the determination of the maximum force that the coupling beams will transfer to the walls due to the formation of plastic hinges at the ends of all coupling beams. The axial force in the walls is calculated as the sum of the capacity-limited coupling beam shear capacity along the height of the structure (added to gravity forces). To determine this axial force, expected flexural capacities of selected and sized coupling beams are calculated, accounting for the material expected strength ( $R_y$  and  $R_c$  factors). These expected capacities are amplified by 1.2 to account for strain hardening in the steel, a biaxial stress state in the steel tension flange (Shafaei et al. 2021a), and concrete confinement.

Conceptualizing this calculation on the theoretical pushover curve, the amplified expected flexural capacity of the coupling beams is associated with the loading at Point B, at which all the coupling beams have formed plastic hinges. Experimental results indicate that the plastic hinge forms over a length equal to approximately one-half the coupling beam depth (Nie et al. 2014). For design, the plastic hinges are considered to form at the ends of the clear span of the coupling beams. The total overturning moment at Point B can be estimated using the total overturning moment at Point A according to

$$\gamma_1 = \frac{\sum_n 1.2 M_{p,\text{exp}}^{cb}}{\sum_n M_u^{cb}} \quad (4)$$

$$\text{OTM}_B = \gamma_1 \text{OTM}_A \quad (5)$$

where  $\sum_n 1.2 M_{p,\text{exp}}^{cb}$  = sum of expected flexural capacities of coupling beams along structure height;  $\sum_n M_u^{cb}$  = sum of flexural design demands for coupling beams along structure height;  $n$  = number of coupling beams along structure height; and  $\text{OTM}_A$  and  $\text{OTM}_B$  = overturning moments at Point A and B, respectively, on theoretical pushover curve.

Returning to calculating the axial force in the wall, the amplified expected moment is converted into the capacity-limited expected shear at the ends of the coupling beam following

$$V_{\text{amp,exp}}^{CB} = \frac{2 \times 1.2 M_{p,\text{exp}}^{CB}}{L_{CB}} \quad (6)$$

where  $L_{CB}$  = clear span length of coupling beam.

This beam end shear is summed along the height of the structure and added to the gravity load in the wall to calculate the capacity-limited axial force in the wall, following Eqs. (7) and (8). One wall will be subjected to axial compression and the other wall will be subjected to axial tension

$$P_{w,CA} = \pm \frac{2.4 \sum M_{p,\text{exp}}^{cb}}{L_{cb}} \quad (7)$$

$$P_{w,\text{exp}} = \pm P_{w,CA} + P_{\text{gravity}} \quad (8)$$

The portion of the total overturning moment resisted by coupling action between the walls is calculated as the equal and opposite axial forces ( $\pm P_{w,CA}$ ) times the distance between them. The remaining portion of the overturning moment is resisted by the composite walls and distributed to them in accordance with their relative flexural stiffnesses [Eqs. (9)–(11)]. Compression and tension walls have different flexural stiffnesses due to the differences in the extent of (uncracked) concrete in compression contributing to the section secant stiffness. The section secant stiffnesses of the walls subjected to axial tension ( $EI_{T\_Wall}$ ) and axial compression ( $EI_{C\_Wall}$ ) can be estimated as the secant stiffness corresponding to 60% of the flexural capacity accounting for the effects of the axial forces (Shafaei et al. 2021b). For example, the section secant stiffness can be obtained from a moment-curvature analysis of the wall considering axial force

$$M_{\text{walls}} = \gamma_1 \text{OTM}_A - P_{w,CA} L_{\text{eff}} \quad (9)$$

$$M_{U\_T\_Wall} = \frac{EI_{T\_Wall}}{EI_{C\_Wall} + EI_{T\_Wall}} \times M_{\text{walls}} \quad (10)$$

$$M_{U\_C\_Wall} = \frac{EI_{C\_Wall}}{EI_{C\_Wall} + EI_{T\_Wall}} \times M_{\text{walls}} \quad (11)$$

where  $L_{\text{eff}}$  = distance between geometric elastic centroid of tension and compression walls;  $EI_{T\_Wall}$  and  $EI_{C\_Wall}$  = effective section stiffnesses of tension and compression walls, respectively; and  $M_{U\_T\_Wall}$  and  $M_{U\_C\_Wall}$  = required flexural strengths for tension and compression walls, respectively.

Finally, the shear forces resisted by the walls for ELF level loads, calculated from elastic analysis, are amplified by a factor of 4 as a conservative approach to account for higher-mode effects and overstrength in the walls from the difference in the design demand (Point B) and the expected flexural capacity (Point C). Applying such a shear amplification factor is consistent with the approach and findings from coupled concrete shear walls (Tauberg et al. 2019).

## Additional Design and Detailing Requirements

In addition to the preceding capacity design approach, several design and detailing requirements are needed to ensure that the composite sections develop their full plastic strength, have adequate ductility, and are sized appropriately for construction concerns such as transportation and standard concrete casting pressures. Such requirements effectively are those prescribed in ASCE 7 (ASCE 2022), and AISC 341-22 (AISC 2022a). These include limits on the reinforcement ratio, plate slenderness, and tie-bar spacing based on the research of Zhang et al. (2014, 2020) and Varma et al. (2019).

Coupling beam requirements similarly are specified to ensure that they behave as intended. First, the existing AISC 360-22 (AISC 2016b) provisions and the upcoming AISC 360-22 (AISC 2022b) and AISC 341-22 (AISC 2022a) provisions apply in this case, including those for the minimum area of steel, compactness criteria, and flexural and shear stiffness values. Second, in addition to these existing requirements, coupling beams must be designed to be flexure-critical. In other words, the ultimate behavior of the beams must be governed by flexural yielding rather than shear strength. As previously discussed, this is because existing test data on composite coupling beams (Nie et al. 2014) indicated greater ductility in flexure-controlled sections. Flexure-controlled coupling beams can be obtained by requiring their length-to-depth ratio to be greater than or equal to 3. Therefore, a range of 3–5 was specified for the archetype structures evaluated in the FEMA P695 study

performed to validate the R factor for these walls (Kizilarlan et al. 2021b), with the upper limit of 5 imposed to ensure meaningful contributions of the coupling beams to the structural system.

More rigorously, to ensure that the coupling beams are flexure-controlled, it is specified that the shear strength of the composite coupling beam must be higher than the capacity-limited shear in the coupling beams due to forming plastic hinges at both ends. This limit is checked using the following equation:

$$V_{n,exp} \geq \frac{2.4M_{p,exp}}{L_{cb}} \quad (12)$$

where  $V_{n,exp}$  = expected shear strength of composite coupling beam calculated per AISC 360-22 (AISC 2022b) Section I4.2 using expected yield strength,  $R_y F_y$  for steel and expected compressive strength  $R_c f'_c$  for concrete [the shear strength equations in AISC 360-22 (AISC 2022b) Section I4.2 are based on Kenarangi et al. (2021a)]; and  $M_{p,exp}$  = expected flexural capacity of composite coupling beam calculated using expected yield strength,  $R_y F_y$ , for steel and expected compressive strength  $R_c f'_c$  for concrete.

Generally, when the coupling beam forms plastic hinges at its ends, the capacity-limited shear in the beam (experienced at the ends) is equivalent to 2 times the plastic moment divided by the member length, but Eq. (12) is more conservative to consider additional capacity from a biaxial (tensile) stress effect in the steel, steel strain hardening, and confinement of the concrete. This additional capacity was discussed by Bruneau et al. (2019), and is similar to that discussed by Shafaei (2020). The shear and flexural strength can be calculated according to the methods prescribed in AISC 360-22 (AISC 2022b) Sections I4.2 and I1.2a, respectively.

Finally, the only coupling beam-to-wall connection details permitted are those able to develop a coupling beam chord rotation capacity of 0.030 rad before flexural strength decreases to 80% of the beam's flexural plastic strength. This requirement is consistent with the models used in the FEMA P695 study (Kizilarlan et al. 2021b) and the rotation capacity seen in tests (Nie et al. 2014; Varma et al. 2021).

## Design Examples

The capacity design procedure and corresponding requirements were demonstrated using a series of design examples. These structures represent typical buildings that could use the CC-PSW/CF system. Building geometry, floor loading, and material properties for the buildings considered are presented in Table 1. These included a typical story height of 4.3 m (14 ft) and floor plan dimensions of 61.0 × 36.6 m (200 × 120 ft). Both planar and C-shaped walls were included in the design examples. The building floor layouts for planar and C-shaped coupled walls are shown in Fig. 2.

**Table 1.** Input parameters for structure design

Parameter	Values	Reasoning
Coupling beam aspect ratio ( $L/d$ )	3, 4, 5	Typical coupling beam aspect ratios
Story height	First story: 5.2 m (17 ft), typical story: 4.3 m (14 ft)	Typical story heights
Seismic weight	Floor load of 5.75 kPa (120 psf)	Estimated from components: steel framing [0.58 kPa (12 psf)]; 2.5-in. normal-weight concrete on 3-in. steel deck [2.39 kPa (50 psf)]; curtain wall [0.72 kPa (15 psf)] on facade area; superimposed dead load [0.72 kPa (15 psf)]; and partitions [0.72 kPa (15 psf)]
Coupled wall length	9.1 m (30 ft)	Typical bay length is 9.1 m (30 ft), set of walls would span the length of a bay
Floor dimensions	36.3 × 61.0 m (120 × 200 ft)	Typical floor geometry

Planar coupled walls generally are appropriate for low- to midrise (up to 15-story) buildings, whereas C-shaped walls are better suited for midrise to high-rise (12–24-story) buildings because the greater seismic loads necessitate additional strength and stiffness. Standard materials were used, namely 41.4 MPa (6,000-psi) normal-weight concrete and A992 steel [345 MPa (50 ksi)].

Structural analysis followed the equivalent lateral force procedure outlined in ASCE 7-16, using design spectra based on the site-specific seismic response parameters for a Seismic design category D earthquake ( $S_{DS} = 1.0$  g and  $S_{D1} = 0.6$  g). The fundamental period was estimated based on the structure type and geometry, with the upper-limit period ( $C_u T_a$ ) used as the initial-period estimate. In these examples, all structural periods obtained from eigenvalue analysis performed using commercially available software (SAP2000 17) were greater than the upper-limit periods. The seismic response coefficient,  $C_s$ , was calculated and used to distribute the seismic forces vertically along the height of the structure. The amplified base shear and overturning moment were calculated based on this distribution. The amplified base shear was taken as the equivalent lateral force base shear multiplied by a factor of 4 to account for higher-mode effects (for reasons mentioned previously).

An assumed coupling ratio was used to distribute the total overturning moment into contributions due to the (1) axial force couple, and (2) individual walls. Initially, the coupling ratio was assumed to be 60%; this value was adjusted, as appropriate, during design iterations. Initial wall and coupling beam dimensions were assumed, and the shear, flexural, and axial stiffnesses were calculated for both wall and coupling beam elements. No recommendations currently exist for initial wall sizes but, through iterations, reasonable wall sizes were determined. The stiffness values then were used in an elastic model with equivalent lateral force procedure loads. As mentioned previously, these stiffness values were developed by Agrawal et al. (2020) by calibrating linear elastic models (with the effective stiffness values) with nonlinear models (with concrete cracking modeled explicitly) subjected to ELF level loads. This model was used to calculate the interstory drift ratio. Finally, the maximum amplified inter-story drift was compared to the code-specified drift limit, in this case, 2% interstory drift per ASCE7-16. If the system met the drift limit, the design process continued; if the system did not meet the drift requirements, the system was resized to bring drift below the acceptable limit.

Next, the coupling beams were designed. The design checks for coupling beams were outlined earlier. The calculated strengths were compared with the required coupling beam strengths (shear and flexure) obtained from the analysis. Coupling-beam geometry requirements including limits on the length-to-depth ratio, flange plate slenderness, and web plate slenderness also were checked. If necessary, the coupling beams were resized, and the preceding analysis was repeated with the new cross sections. Then the

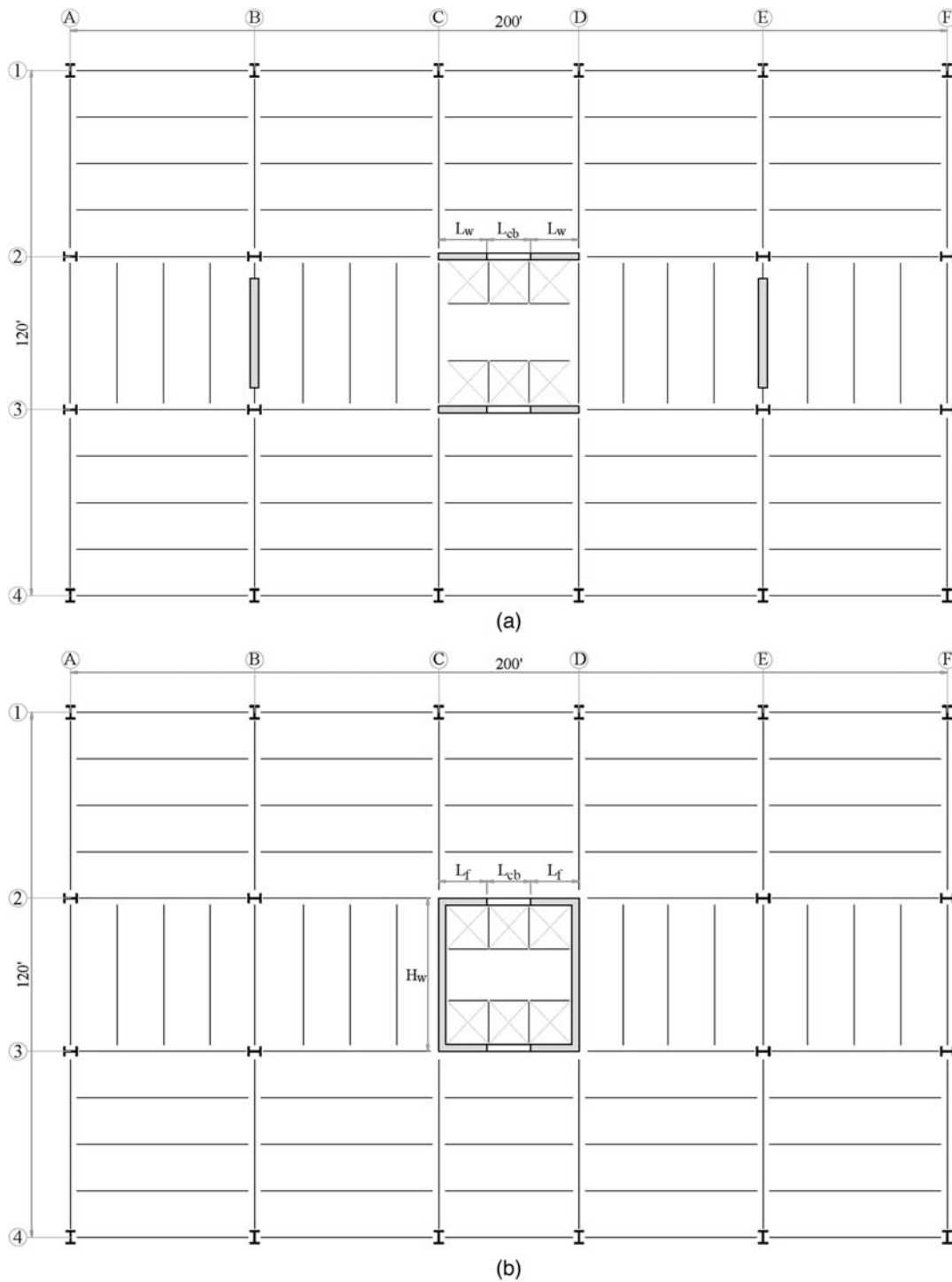


**Fig. 2.** Layout of (a) planar walls; and (b) coupled walls.

composite walls were designed. The shear and axial capacities were compared with the corresponding demands determined from the analysis. The flexure demand was determined based on the capacity design process detailed earlier. This step considered the relative flexural stiffnesses of the tension or compression walls. The flexural demands obtained from capacity design were compared with the flexural capacity of the wall, calculated using the plastic stress distribution method, while accounting for the effects of axial forces (compression or tension). Walls were redesigned if their capacity was less than demand, and reanalyzed for a new iteration. Typically, walls can be redesigned by adjusting geometric parameters

such as the wall length, wall thickness, and steel plate thickness. However, because the wall length often is constrained by architectural requirements, the geometric parameters that were adjusted to redesign the walls were limited to the wall thickness and/or steel plate thickness. Increasing the wall thickness increases stiffness, whereas increasing the steel plate thickness increases strength.

Connection design and detailing issues were beyond the scope of this paper, but would be performed at this point. This would include the connections between the tie bars and steel plates and between C-PSW/CF components, coupling beam-to-wall connections, and wall-to-foundation connections. The requirements for

**Table 2.** Section sizes for coupled planar walls

Stories	$L/d$	$L_w$ [mm (in.)]	$t_{sc}$ [[mm (in.)]	$t_p$ [mm (in.)]	$L_{cb}$ [mm (in.)]	Coupling beam section [mm (in.)]
8	4	3,350 (132)	610 (24)	14.3 (9/16)	2,440 (96)	24 × 24, 1/2(f), 3/8(w) [610 × 610, 12.7(f), 9.5(w)]
12	3	5,180 (204)	457 (18)	14.3 (9/16)	1,830 (72)	18 × 24, 5/16(f), 3/8(w) [457 × 610, 7.9 (f), 9.5(w)]

**Table 3.** Section sizes for CC-shape walls

Stories	$L/d$	$H_w$ [mm (in.)]	$L_f$ [mm (in.)]	$t_{sc,f}$ [mm (in.)]	$t_{sc,w}$ [mm (in.)]	$t_p$ [mm (in.)]	$L_{cb}$ [mm (in.)]	Coupling beam section [mm (in.)]
18	5	9,140 (360))	3,960 (156))	660 (26))	406 (16))	14.3 (9/16) ()	3,050 (120)	26 × 24, 1/2(f), 3/8(w) [610 × 610, 12.7(f), 9.5(w)]
22	4	9,140 (360))	4,880 (192))	610 (24))	356 (14))	12.7 (1/2))	2,440 (96)	24 × 24, 7/16(f), 3/8(w) [610 × 610, 11.1(f), 9.5(w)]

**Table 4.** Summary of important structure design to demand ratios

Stories	$C_u T_a$ (s)	$T_n$ (s)	Ratio of $\phi M_n$ to $M_u$ , compression wall	Ratio of $\phi M_n$ to $M_u$ , tension wall	$\phi V_n/V_{base}$	Ratio of $V_{n,exp}$ to $(2.4M_{p,exp})/L_{cb}$ for coupling beams	IDR <sub>max</sub> (%)
8	0.98	1.42	1.3	1.2	3.6	1.1	1.4
12	1.32	1.83	1.7	1.8	4.7	1.2	1.3
18	1.78	2.98	6.0	6.6	2.9	1.3	1.9
22	2.07	3.60	1.8	1.9	2.6	1.2	2.4

these connections are specified in AISC 341-22 (AISC 2022a). Tie-to-plate connections are required to be detailed to develop the full tensile strength of the tie bar. C-PSW/CF components (between steel web plate and flange plates) are required to be complete joint penetration welds. Coupling beam-to-wall connections need to develop the rotation capacity and strength described in the coupling beam requirements section. Wall-to-foundation connections are to be designed to resist 1.1 times the expected plastic composite flexural strength of the wall. This requirement for wall-to-foundation connections is in accordance with AISC 341-16 Section H7. This 1.1 factor is included to prevent failure of the foundation connection prior to development of the wall plastic hinge.

The properties of four resulting example structures designed per the preceding procedure are presented in Tables 2 and 3. These properties include the length of the planar wall,  $L_w$ ; length of the C-shaped wall web,  $H_w$ ; length of the C-shaped wall flange,  $L_f$ ; total wall thickness,  $t_{sc}$ ; plate thickness,  $t_p$ ; and coupling beam length,  $L_{cb}$ . These properties were chosen to be in the practical range for building construction while meeting the controlling limit states (drift or strength) without introducing significant over-strength (plastic strength-to-required strength ratio). Table 4 summarizes the relevant structural performance markers.

## Finite-Element Modeling

These example structures were modeled using multiple approaches: a two-dimensional (2D) finite-element model in Abaqus version 2017, and two independently calibrated fiber-based models in OpenSees version 2.5.0. This approach was used because the finite-element model directly calculated and illustrates numerous failure modes (including local buckling, shear yielding, and effects of confinement), whereas the fiber-based model was computationally efficient and able to simulate expected failure modes (such as coupling beam failure, cyclic degradation of steel, and steel fracture). All these models were benchmarked independently to planar and C-shaped C-PSW/CF walls and coupling beams tests (Kizilarlan et al. 2021a; Kenarangi et al. 2021b; Shafaei et al.

2021a). These benchmarking studies were presented in detail by Bruneau et al. (2019), and are not repeated here for brevity.

## 2D Abaqus Model

The 2D Abaqus model consisted of finite-element components for all beam and wall elements. The walls were modeled with four-node composite shell sections with reduced integration (S4R) to represent the infill concrete core and web plates, and with two-node truss element (T3D2) to represent the steel flange plates. The coupling beams similarly were modeled with layered composite shell elements (S4R) for infill concrete and web plate and truss element (T3D2) for coupling beam flange plates. Additionally, a leaning column with gravity loads was modeled using truss elements (T3D2) to represent the  $P$ -delta effects on the structure. The steel and concrete material models used in this analysis were based on effective stress–strain curves developed by Shafaei et al. (2021a) from a three-dimensional (3D) finite-element model benchmarked to C-PSW/CF testing. These effective stress–strain curves were used to implicitly account for the effects of the biaxial stress state in the steel and confinement in the concrete.

The behavior of the 2D Abaqus wall model was benchmarked to tests performed by Shafaei et al. (2021a). The detailed 3D finite-element, 2D finite-element, and experimental results for one of the benchmarking experiments for the walls are shown in Fig. 3. This analysis showed that the effective stress–strain curve implementation in the 2D model can capture very similar behavior to the more robust 3D model. This 2D finite-element model is computationally efficient for analyzing multistory buildings. The 3D and 2D finite-element models also accurately can simulate the cyclic behavior of the experimental test including the lateral stiffness, capacity, post-peak degradation, and fracture failure of the steel plates. However, due to limitations in the concrete damage model, the pinching observed in the experiment was not captured accurately; the cyclic comparisons were reported in full by Shafaei et al. (2021a).

A similar process was repeated for coupling beam elements, and associated stress–strain curves for these elements also were extracted and implemented in the 2D finite-element model. This analysis was benchmarked to the flexural critical tests discussed by

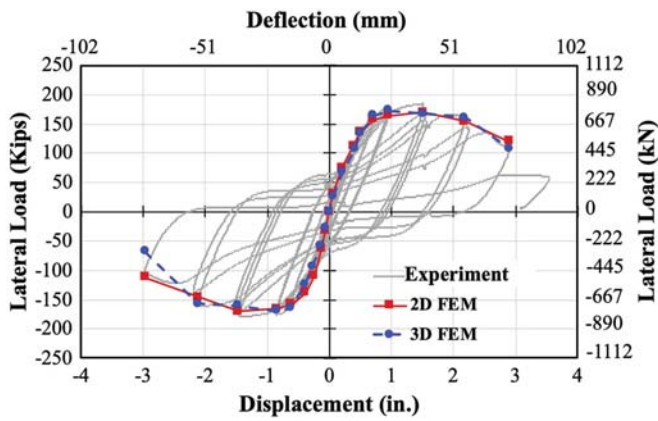


Fig. 3. Finite-element results from 3D and 2D models.

Nie et al. (2014) and Varma et al. (2021). Further test details on this benchmarking process were presented by Bruneau et al. (2019).

### OpenSees Models

The OpenSees models consisted of fiber elements representing beam and wall sections. The first OpenSees model relied on implementing the effective stress–strain curves in OpenSees and modeling coupling beams with concentrated plasticity elements, whereas the second model used material models natively available in OpenSees and modeled coupling beams with distributed plasticity elements. Analyzing the example structures using differing fiber-based modeling approaches adds additional certainty to the behavior if the analytical models produce similar results.

In the first model, referred to herein as the concentrated plasticity (CP) model, walls were modeled with nonlinear fiber elements from the base of the wall to a height equal to the length of the wall. These nonlinear fiber elements used the same steel and concrete effective stress–strain curves as the Abaqus walls. These stress–strain curves were implemented in OpenSees using ReinforcingSteel and Concrete02 to model the steel and concrete behavior, respectively. ReinforcingSteel was chosen because it could simulate cyclic degradation and nonsymmetric tension and compression behavior (to simulate local buckling of steel plates in compression). Concrete02 was chosen because it adequately captured crack closure and had a higher rate of convergence than other alternatives tried. Wall elements above the nonlinear section were assigned cracked transformed elastic properties. Nonlinear properties used for wall steel and concrete are presented in Tables 5 and 6, respectively.

Coupling beam elements were modeled with nonlinear concentrated plasticity elements at both ends representing the flexural plastic hinge behavior. This concentrated plasticity element used a Modified Ibarra–Medina–Krawinkler deterioration model with bilinear hysteretic response material to capture the cyclic behavior of coupling beam elements. Although this model has the capability of capturing nonsymmetric behavior in the push and pull cycles, the coupling beams' behavior was considered to be symmetric because the sections were compact, resulting in uniform properties in the push and pull directions. The concentrated plasticity elements were connected with elastic elements assigned elastic properties. Concentrated plasticity parameters are presented in Table 7.

For dynamics analysis, the structure was assigned a damping ratio of 5%. This damping was implemented using Rayleigh damping and enforcing mass and stiffness coefficients according to the first two natural periods of the structure. This was implemented as mass and stiffness–proportional damping based on the first and second

Table 5. Steel material properties used for planar wall benchmarking

Parameter	Value
Elastic modulus, $E_s$ [ksi (MPa)]	29,000 (200,000)
Strain hardening ratio, $b$	0.01
Tangent at strain hardening, $E_{sh}$ [ksi (MPa)]	290 (2,000)
Yield stress, $F_y$ [ksi (MPa)]	50 (345)
Ultimate stress, $F_u$ [ksi (MPa)]	65 (448)
Strain at initiation of strain hardening, $\epsilon_{sh}$	$2F_y/E_s$
Strain at ultimate stress, $\epsilon_{ult}$	0.1
Slenderness ratio, $L_{sr}$	10
Buckled stress amplification factor, $\beta$	1
Buckling reduction factor, $r$	0.65
Buckling constant, $\gamma$	0.5
Coffin–Manson constant C, $C_f$	0.6
Coffin–Manson constant a, $\alpha$	0.5
Cyclic strength reduction constant, $C_d$	0.35

Table 6. Concrete material parameters for planar wall benchmarking

Parameter	Value
Compressive strength, $f'_c$ [ksi (MPa)]	6.0 (41)
Strain at maximum strength, $e_{psc0}$	0.0022
Crushing strength, $F_{pcu}$	$0.6f'_c$
Strain at crushing strength, $e_{psu}$	0.008
Tension softening stiffness, $E_{ts}$	$0.1f'_c$
Strain at tensile strength, $e_t$	$8 \times 10^{-5}$
Ratio between unloading slope at $e_{psc0}$ and initial slope, $\lambda$	0.1

Table 7. Parameters used to model behavior of coupling beams with concentrated plasticity elements

Parameter	Value
Elastic stiffness, $K_0$ [kN-m/rad (kip-in./rad)]	
Planar walls (8 and 12 stories)	$2.8 \times 10^6$ ( $2.5 \times 10^7$ )
C-shaped walls (18 and 22 stories)	$5.6 \times 10^6$ ( $5.0 \times 10^7$ )
Strain hardening ratio, $a_s$	0.005
Yield moment, $M_y$ [kN-m (kip-in.)]	
8-story	2,710 (24,000)
12-story	1,810 (16,000)
18-story (two coupling beams)	5,620 (49,700)
22-story (two coupling beams)	4,980 (44,100)
Precapping rotation, $\theta_p$ (rad)	0.025
Post-capping rotation, $\theta_{pc}$ (rad)	0.04
Ultimate rotation capacity, $\theta_u$ (rad)	0.05
Cyclic deterioration parameter for strength deterioration, $\lambda_s$	0.5
Cyclic deterioration parameter for postcapping strength deterioration, $\lambda_C$	1.0
Cyclic deterioration parameter for accelerated reloading stiffness deterioration, $\lambda_A$	1.0
Cyclic deterioration parameter for unloading stiffness deterioration, $\lambda_K$	1.0
Residual strength ratio, Res	0.25
Rate of cyclic deterioration, $D$	1
Rate of strength deterioration, $c_s$	1.0
Rate of postcapping strength deterioration, $c_C$	0.0
Rate of accelerated reloading deterioration, $c_A$	1.0
Rate of unloading stiffness deterioration, $c_K$	1.0
Elastic stiffness amplification factor, nFactor	0
Ratio of reloading stiffness, $A_{pinch}$	1

**Table 8.** First and second structural periods for CP and DP models

Stories	First period,	Second period,	First period,	Second period,
	$T_1$ (s) CP model	$T_2$ (s), CP model	$T_1$ (s), DP model	$T_2$ (s), DP model
8	1.1	0.26	1.05	0.26
12	1.4	0.32	1.38	0.31
18	2.7	0.59	2.05	0.48
22	3.3	0.71	2.56	0.58

periods of the structure. The periods for each example structure are reported in Table 8. Parameters used in the benchmarking models were similar to these but accounted for the actual yield and ultimate strengths of the steel and the nominal strength of the concrete. Further information about the benchmarking of these models and comparisons with the remainder of the tests were given by Bruneau et al. (2019).

In the second model, referred to herein as the distributed plasticity (DP) model, for walls, the nonlinear beam column elements were assigned only to the first story of the walls, and the rest of the stories were modeled using elastic beam-column elements with effective stiffness per AISC 341-22 (AISC 2022a) mentioned previously. The coupling beams were all modeled using distributed-plasticity nonlinear beam-column elements. The nonlinear elements were assigned to the centroid of composite wall cross sections as they were calibrated. To simplify analysis, only half of each building (and thus half of the C-shaped walls) was modeled due to symmetry, but all results are presented for full buildings. Leaning columns were added to the structural model to capture the  $P$ - $\Delta$  effects due to the story gravity loads that were not acting on the CC-PSW/CF system itself. These columns were modeled using elastic beam-column elements. The moments of inertia and cross-section area of the elastic beam-column elements should be multiplied to represent the number of leaning columns assumed to exist in the archetype structure. Because there was no definitive information on the number of leaning columns in the archetype design, these values were chosen arbitrarily to provide insignificant flexural stiffness. Tributary loads coming to the C-PSW/CF walls were applied to the walls on each floor. Rigid links were assigned between the C-PSW/CF wall center of gravity and the point at which the coupling beams framed into the walls, and rigid beams were used to connect the leaning column and C-PSW/CF wall at every floor. These rigid beams were modeled using elastic (almost rigid) truss elements. No seismic mass was assigned to the leaning columns. Seismic masses were applied to the C-PSW/CF walls and distributed equally to their left and right joints at every story. Rayleigh damping was used with a value of 5% damping specified for the first and second periods of vibration. The sensitivity of results to other damping ratios was considered and discussed by Kizilarlan et al. (2021b).

## Seismic Behavior

### Pushover Behavior

The finite-element and fiber models were subjected to pushover analysis. Following the procedure defined in ASCE 41 (ASCE 2017), the structures were subjected to an increasing lateral load distributed according to their first mode response. The behavior in the pushover response followed the capacity design principles: namely yielding of the coupling beams around the equivalent lateral force level loads, yielding of the walls near the loading level at

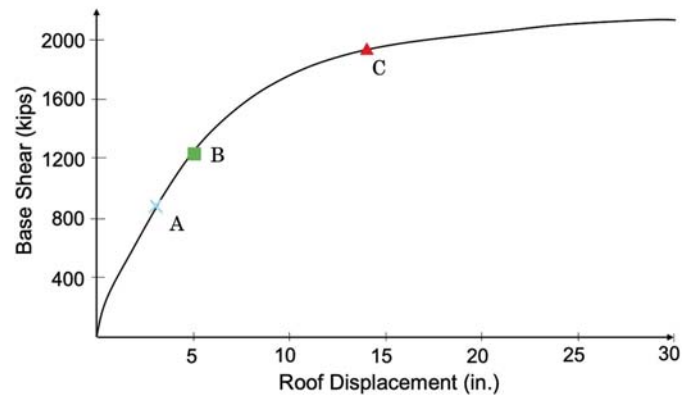


**Fig. 4.** Representative finite element (Abaqus) results for 8-story structure.

which all coupling beams yielded, and fracture of coupling beams preceding fracture in the walls. For example, Fig. 4 shows the characteristic base shear–roof displacement response obtained from conducting a static pushover analysis of a nonlinear inelastic finite element model of an 8-story structure design. Behavior milestones are marked along the pushover response, and the corresponding stress states (emphasizing the extent of yielding) are included in Fig. 5.

Similar results were obtained from the fiber analysis models. The milestones identified from these analyses included (1) first coupling beam yields, (2) last coupling beam yields, (3) wall yields, and (4) coupling beam fracture. For the CP model, coupling beam yielding was identified as the point at which the coupling beam moment exceeded the specified yield moment ( $M_p$ ) value. Coupling beam yielding then spread along the height of the structure. When all coupling beams reached  $M_p$ , this event was marked as the last coupling beam yields milestone. For the DP model, coupling beam yielding was identified as when the extreme fiber strain exceeded the specified yield strain value. For both models, wall yielding was identified when the stress in the extreme fibers in the wall section exceeded the yield stress ( $F_y$ ). A coupling beam fracture occurred when the first coupling beam began to maintain a lower load than the ultimate load.

Fig. 6 shows the base shear versus roof displacement responses obtained from the nonlinear static pushover analyses of the 8-, 12-, 18-, and 22-story structures conducted using both fiber-based (CP and DP) models. These plots consistently show the equivalent lateral force level and yielding of the first coupling beam close to one another. Next, the last coupling beams yielded. This milestone was followed by yielding in the walls, and finally coupling beam fracture. These pushover analysis curves from both the CP and the DP models were similar for all four example structures, and the initial milestones were shown to occur at similar displacements, except the DP model exhibited a more ductile postpeak behavior with a longer and gentler descending branch. This extended ductility occurred because the material models used were benchmarked to cyclic (hysteretic) component behavior and used cumulative plastic strains to model fracture failure (Kizilarlan et al. 2021a). The fracture-initiating cumulative plastic strain values therefore were reached only at large displacements during the monotonic pushover analyses. On the other hand, the CP model used the envelope of the cyclic hysteretic behavior to define the moment-rotation behavior of the concentrated plastic hinges at the ends of the coupling beam elements. Consequently, the concentrated plastic hinges were programmed to undergo fracture failure at a rotation of 0.03 rad, irrespective of cumulative inelastic strain history. This event (indicated with a solid triangle on the pushover response

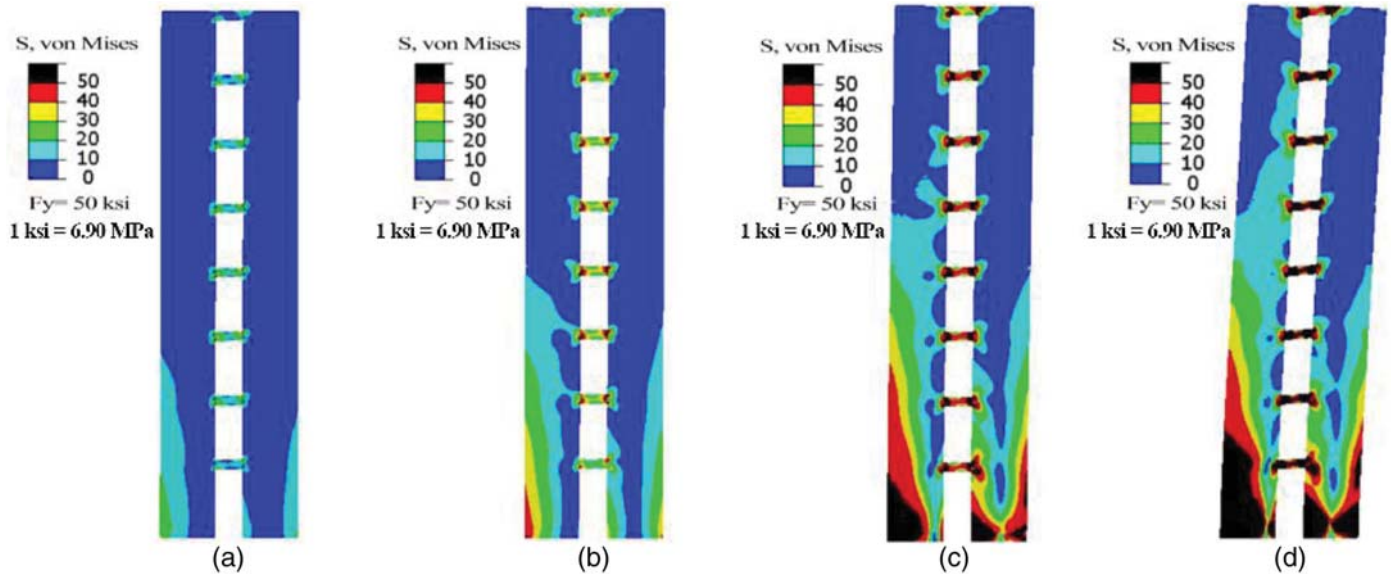


**Fig. 5.** Finite-element milestones for 8-story structure: (a) ELF; (b) all coupling beams yield; (c) plastic mechanism with all coupling beams and wall yielding; and (d) fracture of beams and walls.

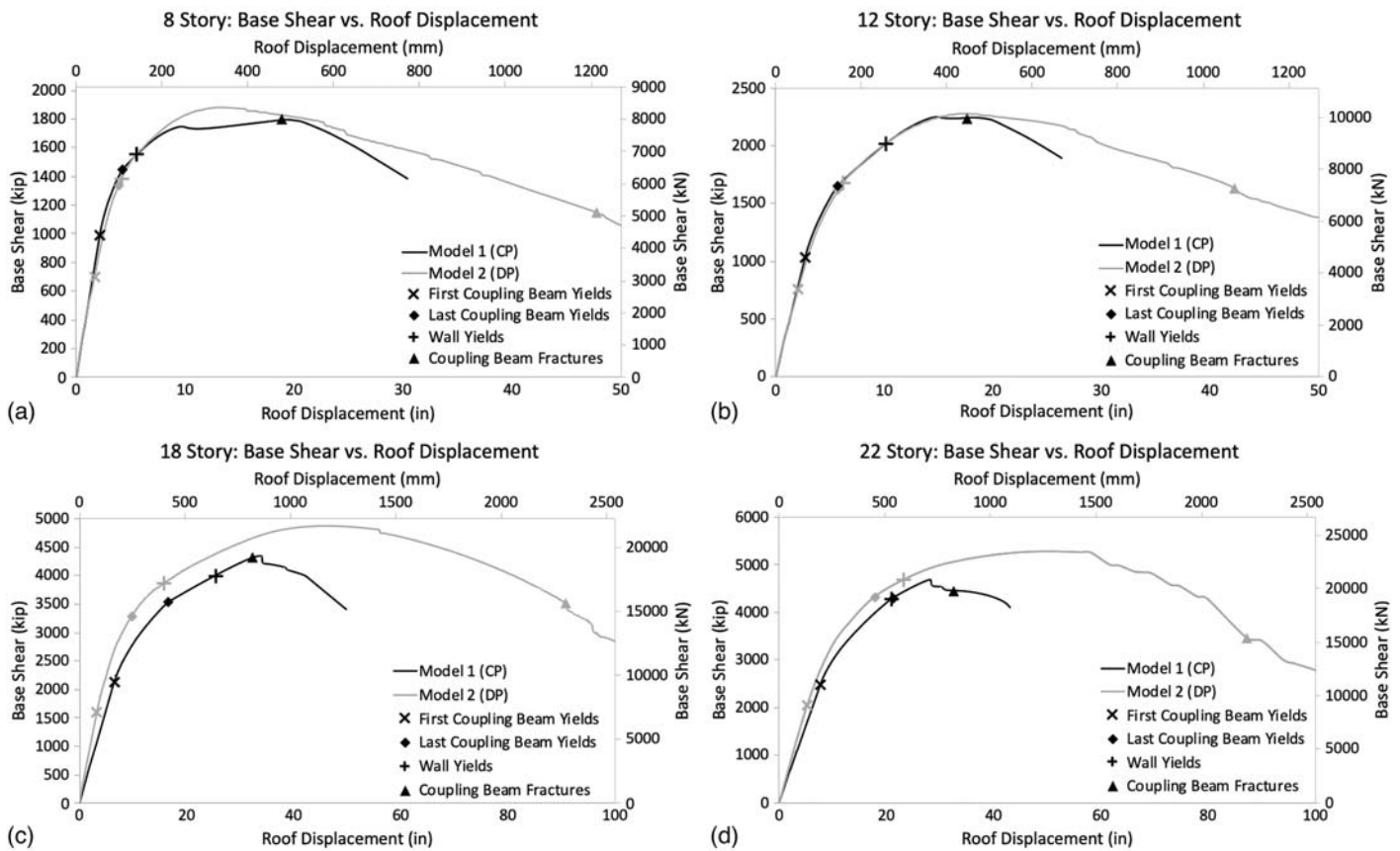


**Fig. 6.** Fiber analysis (CP and DP model) pushover results for 8-, 12-, 18-, and 22-story example structures.

plots) demarcates the deviation in the postpeak responses from the two models.

From the pushover response, values for  $\gamma_1$ ,  $\gamma_2$ , and  $\Omega_0$  were calculated, and are presented in Tables 9 and 10 for the CP and DP models, respectively. These values were close to each other and to the calculated design values [Eq. (4)] despite differences in

modeling approach. In addition to exploring the overstrength of the system, the coupling ratio and axial load in the walls also were investigated. These two parameters measure the behavior of the coupling beams relative to that of the rest of the structure. The coupling ratio represents the portion of the total overturning moment that is resisted by the axial load in the walls applied by the coupling

**Table 9.** Capacity design overstrength values from analysis and calculations from CP model

Stories	$\gamma_1$ , Eq. (4)	$\gamma_1$ , analysis	$\gamma_2$ , analysis	$\Omega_0$ , analysis	$\gamma_1$ (analysis)/ $\gamma_1$ [Eq. (4)]
8	1.91	1.77	1.16	2.04	0.93
12	1.81	2.06	1.11	2.29	1.14
18	1.76	1.84	1.09	2.00	1.05
22	1.46	1.88	1.09	2.05	1.29

**Table 10.** Capacity design overstrength values from analysis and calculations from DP model

Stories	$\gamma_1$ , Eq. (4)	$\gamma_1$ , analysis	$\gamma_2$ , analysis	$\Omega_0$ , analysis	$\gamma_1$ (analysis)/ $\gamma_1$ [Eq. (4)]
8	1.91	1.57	1.36	2.14	0.82
12	1.81	1.71	1.45	2.49	0.93
18	1.76	1.77	1.26	2.24	1.01
22	1.46	2.05	1.13	2.31	1.38

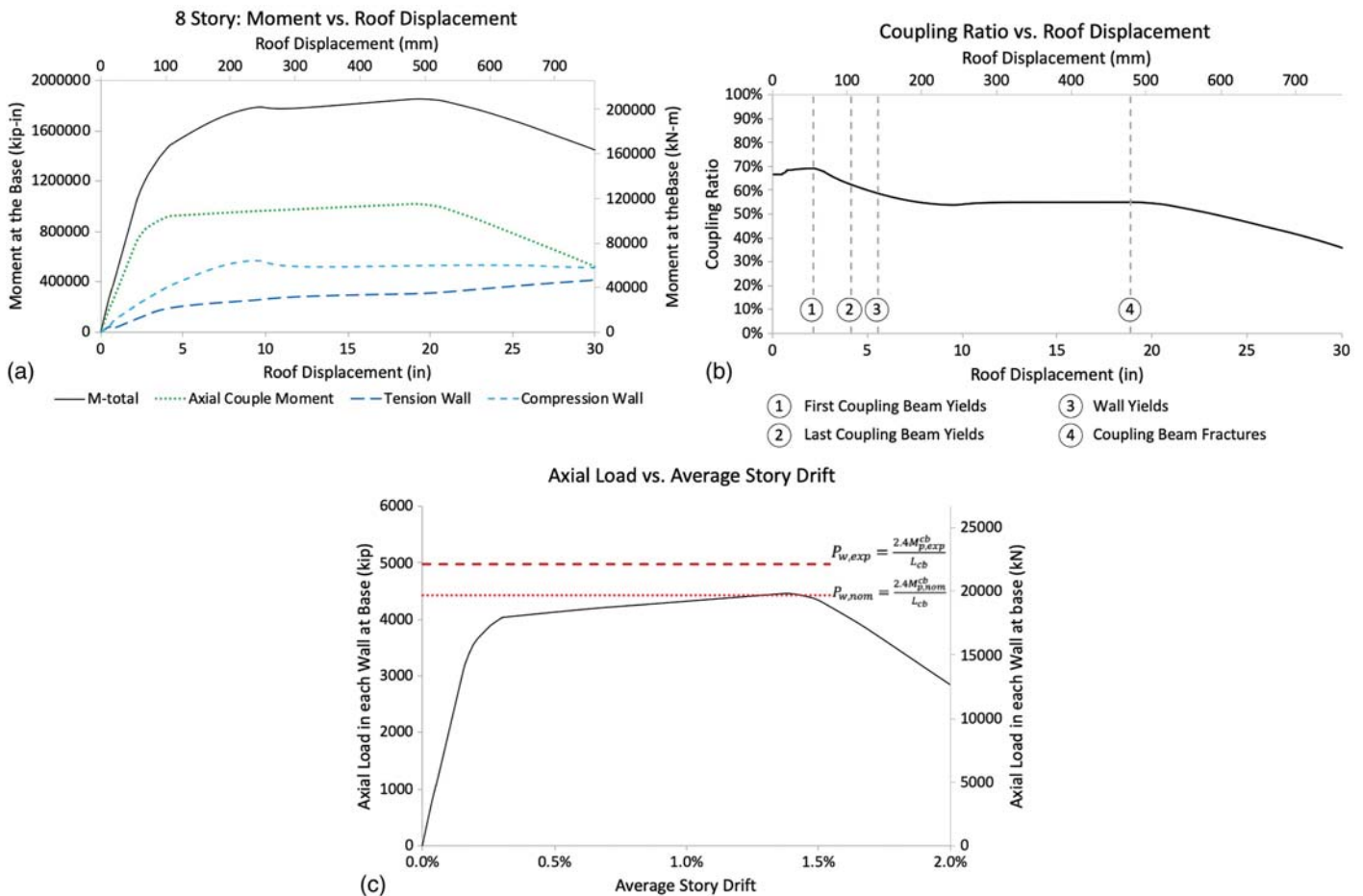


**Fig. 7.** CP model pushover response for 8-story structure (a) moment versus roof displacement including axial couple contribution, tension wall, and compression wall; (b) coupling ratio versus roof displacement; and (c) axial load versus average story drift considering  $P_{w,nom}$  and  $P_{w,exp}$  limit.

beam end shears. This behavior was investigated by examining the results from the 8-story structure. Figs. 7(a and b) divides the total overturning moment into portions resisted by the individual walls, and the axial force couple caused the coupling beams. In Fig. 7(b), the contribution from the axial force couple is normalized by the total overturning moment to calculate the coupling ratio. Together, these plots show that the coupling ratio varied with additional drift. Initially, the coupling ratio was about 65%, but this value decreased

to 55% as the coupling beam contribution to the axial load leveled out and the moment in the individual walls continued to increase.

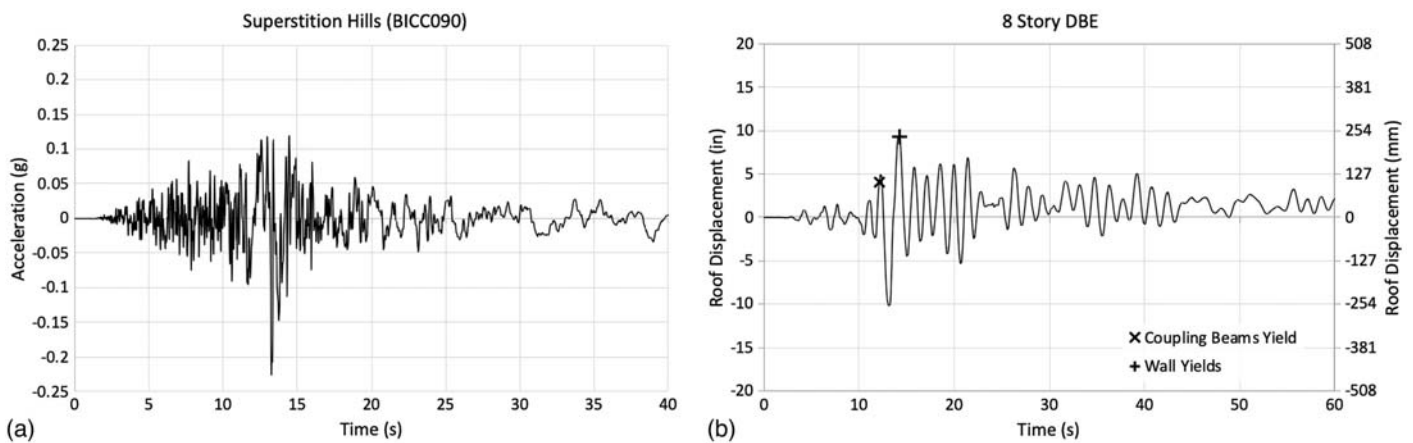
The capacity-limited axial load in the axial walls was evaluated by comparing the maximum axial load in the wall (from the analysis) with the capacity limited load from the initial design. For the 8-story structure, the axial load in the walls varied as the displacement increased [Fig. 7(c)]. This change occurs as all the coupling beams yield and undergo strain hardening. According to the capacity

**Table 11.** Comparison of capacity limited axial load and axial load seen in pushover analysis

Stories	$P_{w,nom}$ [kN (kip)], Eq. (13)	$P_{w,exp}$ [kN (kip)], Eq. (8)	$P_w$ , analysis [kN (kip)], CP model	$P_w$ , analysis [kN (kip)], DP model	$P_w/P_{w,nom}$ , CP model	$P_w/P_{w,nom}$ , DP model
8	19,700 (4,420)	22,000 (4,940)	19,900 (4,470)	20,600 (4,640)	1.01	1.05
12	25,900 (5,820)	29,200 (6,570)	27,700 (6,230)	29,500 (6,630)	1.07	1.14
18	74,800 (16,800)	83,500 (18,800)	72,500 (16,300)	78,300 (17,600)	0.97	1.05
22	100,000 (22,600)	112,000 (25,200)	99,200 (22,300)	108,000 (24,200)	0.99	1.07

**Table 12.** Ground motions used to analyze time-history response of structures

Earthquake	Year	Magnitude	Recording station	PEER NGA database information
Superstition Hills	1987	6.5	El Centro Imp. Co.	SUPERST/B-ICC090
Loma Prieta	1989	6.9	Gilroy Array #3	LOMAP/G03000
Northridge	1994	6.7	Canyon Country-WLC	NORTHR/LOS270
Kobe	1995	6.9	Nishi-Akashi	KOBE/NIS090

**Fig. 8.** (a) Superstition Hills acceleration versus time ground motion; and (b) finite-element (Abaqus) results for the 8-story structure subjected to the design basis earthquake.

design philosophy, the maximum axial load in the wall can be estimated according to Eq. (8). However, because the analysis models used nominal material properties instead of expected values, the Eq. (8) estimate for the axial load in the wall exceeded the actual load level from the analysis. If instead the axial load in the walls was estimated using the nominal capacity of the coupling beams [Eq. (13)], then it closely matched the maximum axial load in the walls. Table 11 compares this axial load level in the walls for both the CP and DP analysis models

$$P_{w,nom} = \frac{2.4M_{p,nom}^{cb}}{L_{cb}} + P_{gravity} \quad (13)$$

### Nonlinear Time-History Response

Nonlinear time-history analysis was performed for the design basis earthquake (DBE), maximum considered earthquake, and failure-level earthquake (FLE). This evaluation was performed to verify that the nonlinear dynamic response of the designed archetype generally was in accordance with the capacity design principle implemented while proportioning and designing the structure. Ground motions were considered in one direction, and the record intensity was scaled up until failure occurred. Failure was defined conservatively as the point at which the structure reached and exceeded 5%

interstory drift ratio. The corresponding ground motion intensity was referred to as the failure-level earthquake. Table 12 lists the ground motions for which each structure was analyzed. These ground motions were selected because they all represented strong, far-field motions of various durations, magnitudes, and locations. Although each structure was analyzed for all the ground motions, the following discussion focuses on the response of each structure for only one ground motion, because the observed responses were consistent.

First, the behavior of the 8-story structure was investigated using the Abaqus finite-element model. This model was subjected to the ground motions scaled to the spectral acceleration levels corresponding to the design basis earthquake, maximum considered earthquake, and failure-level earthquake. The analysis results for the DBE-level earthquake are shown in Fig. 8, and a breakdown of the milestones observed is shown in Fig. 9. Under the design-level earthquake, the structure experienced yielding in the coupling beams first, followed by yielding at the base of the wall. Yielding spread along the height of the structure, with all coupling beams undergoing some plastification. No fracture failures were observed. Similarly, for the maximum considered earthquake (Figs. 10 and 11), the first milestone was coupling beam yielding, followed by yielding in the walls. The propagation of yielding (Fig. 11) was greater than the yielding observed for the DBE

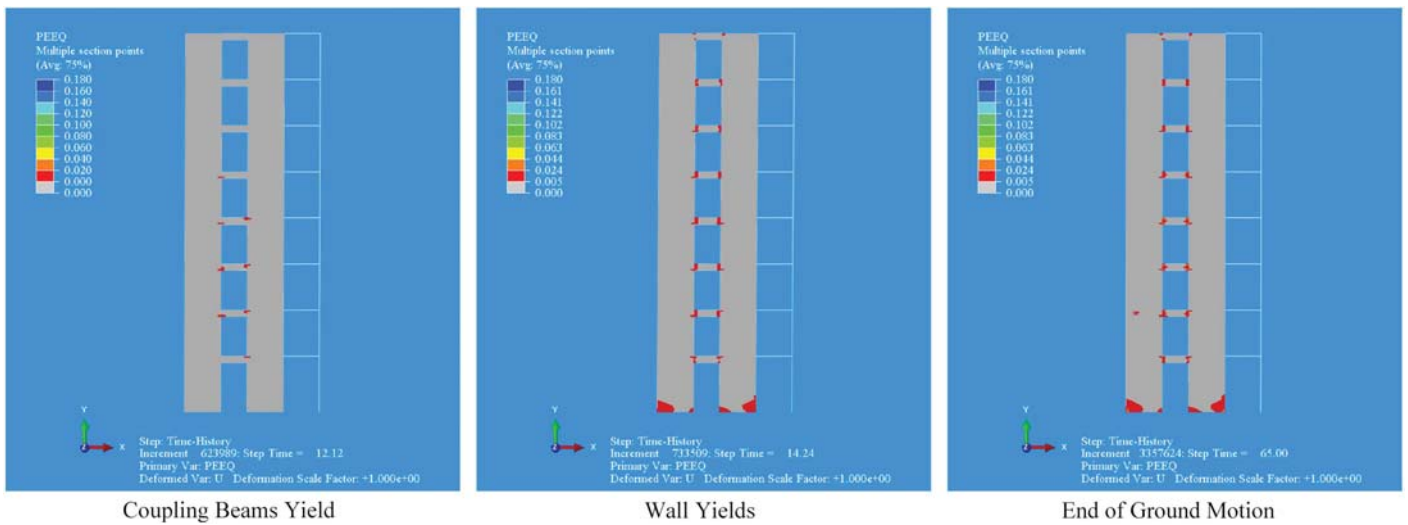


Fig. 9. Milestones observed in the DBE finite element analysis of the 8-story structure.

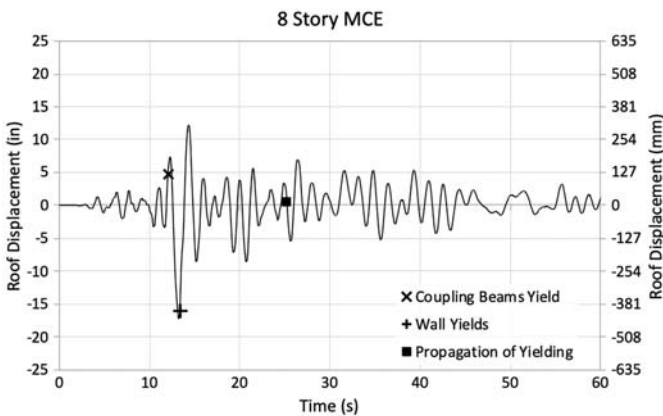


Fig. 10. Finite-element (Abaqus) results for the 8-story structure subjected to the maximum considered earthquake.

earthquake, but did not include any fracture failure. Finally, the failure-level earthquake (with ground accelerations over 4 times the DBE ground accelerations) caused the structure to experience all anticipated milestones. These results are shown in Figs. 12 and 13. The coupling beams yielded, followed by yielding in the wall, as observed in the DBE and MCE analysis. Next, fracture initiated in the coupling beams, and finally, fracture occurred in the walls. The progression of events generally was in accordance with the capacity design principle, indicating that the structure was proportioned properly to follow the prescribed mechanisms.

The CP and DP models in OpenSees were used to simulate the seismic responses of all structures to the DBE, MCE, and FLE. Similar to the analyses conducted using the Abaqus finite-element models, the focus was on identifying performance milestones and observing whether the nonlinear dynamic response was in accordance with the capacity design principle. The results for the 8-story structure are shown in Fig. 14 for both models. For the DBE, the first milestone was yielding of the first coupling beam.

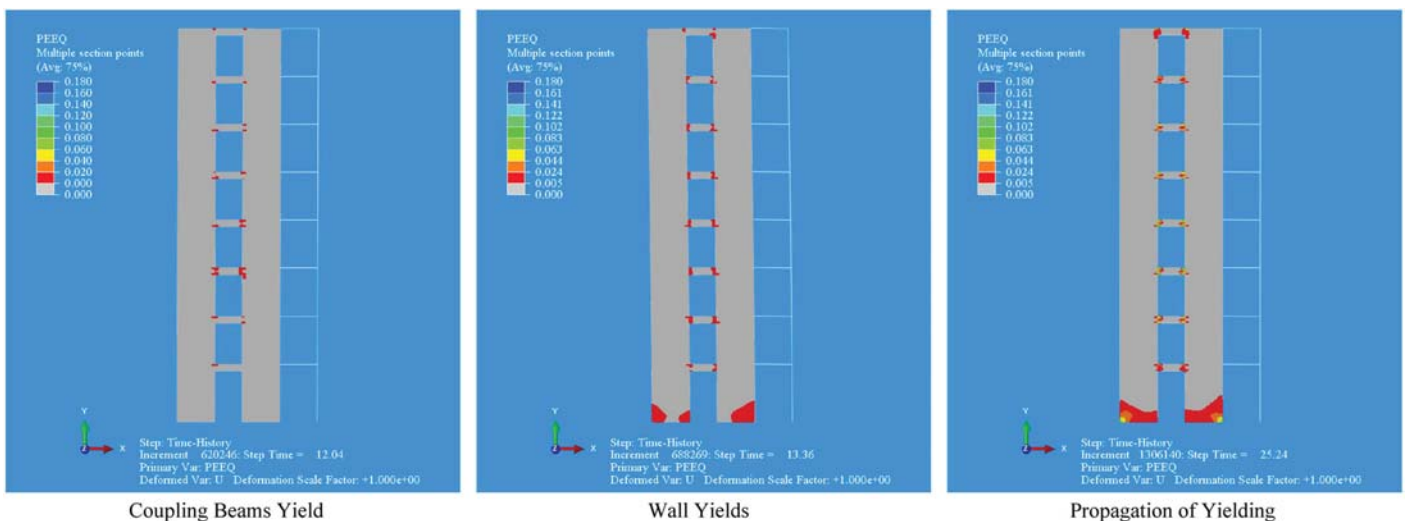
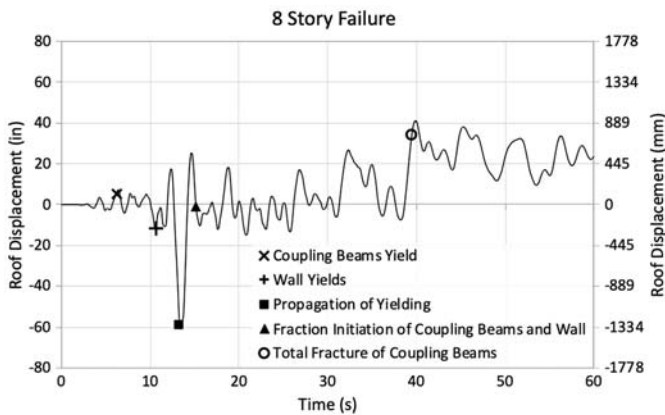


Fig. 11. Milestones observed in MCE finite-element analysis of the 8-story structure.

This milestone was followed by the yielding of all coupling beams. The final milestone was yielding of the wall. For both models, the milestones observed in this analysis were similar to those observed from the Abaqus analysis, although they occurred

at slightly different times, except that initiation of wall yielding was not observed with the DP model. Rather, wall yielding with the DP model was observed first during the MCE analysis. The MCE analysis included an additional milestone—fracture in the coupling beams for the CP model. This fracture was not seen in the Abaqus model, which reiterates that the CP model is more conservative than other models, including the finite-element model. The FLE added failure of all coupling beams to the milestones for both models. After the failure of the last coupling beam, the structure appeared to have a significantly different effective period, as indicated by the long period response during the second half of the ground motion. This change in the effective period is most evident by comparing the analysis results from the DBE and MCE earthquakes after the first 20 s of the ground motion. The FLE had a few high-amplitude cycles with longer duration than the numerous lower amplitude cycles observed in the DBE and MCE analysis.

The analysis results for the 12-, 18-, and 22-story structures showed similar performance milestones and confirmed that the nonlinear dynamic responses generally were in accordance with the capacity design principle. These results are shown in Figs. 15–17 for both the CP and DP models. For the sake of brevity, only the analysis results that deviated slightly from the expected progression



**Fig. 12.** Finite-element (Abaqus) results for the 8-story structure subjected to the failure-level earthquake.

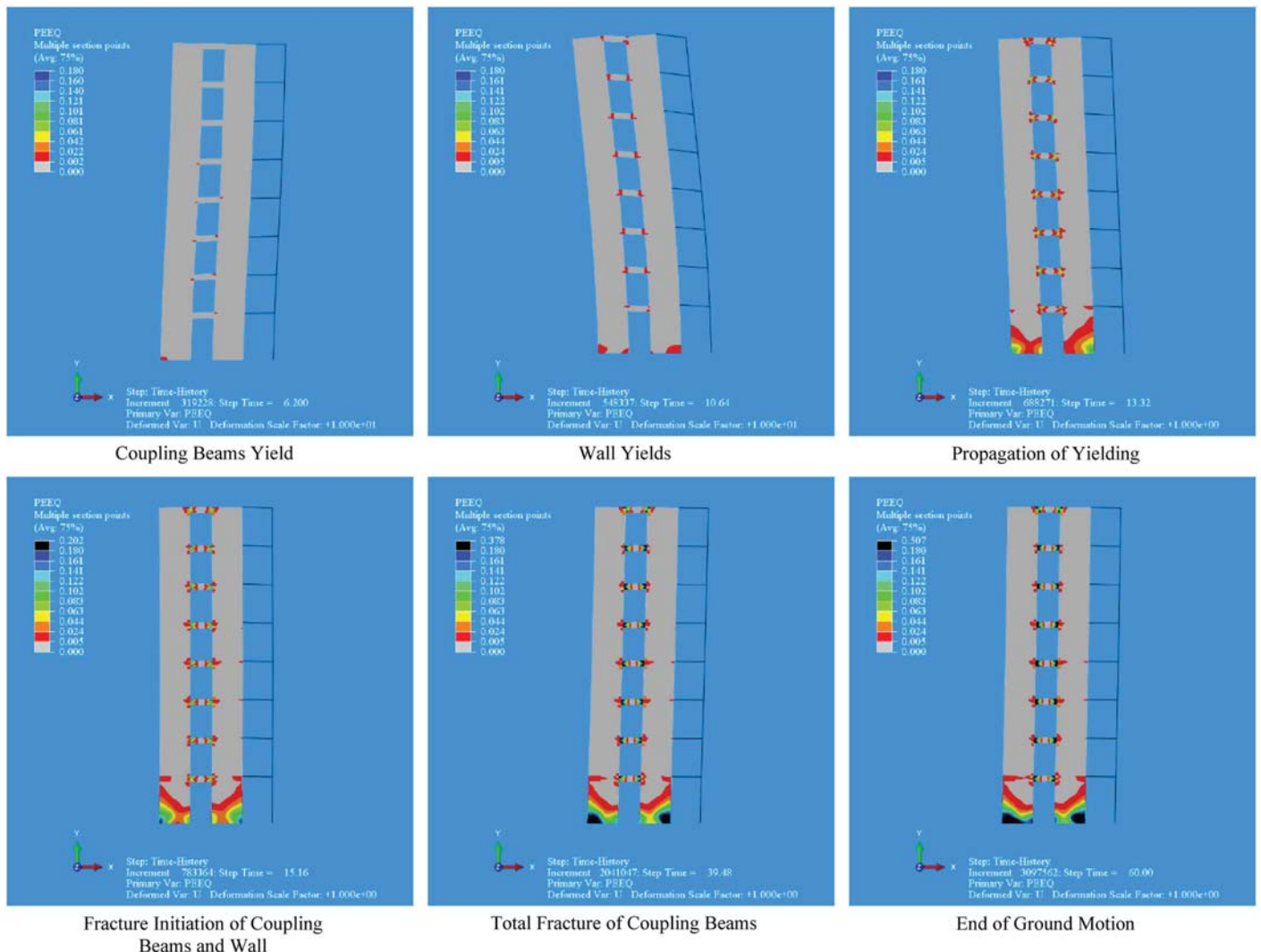


**Fig. 13.** Milestones observed in failure-level finite-element analysis of the 8-story structure.

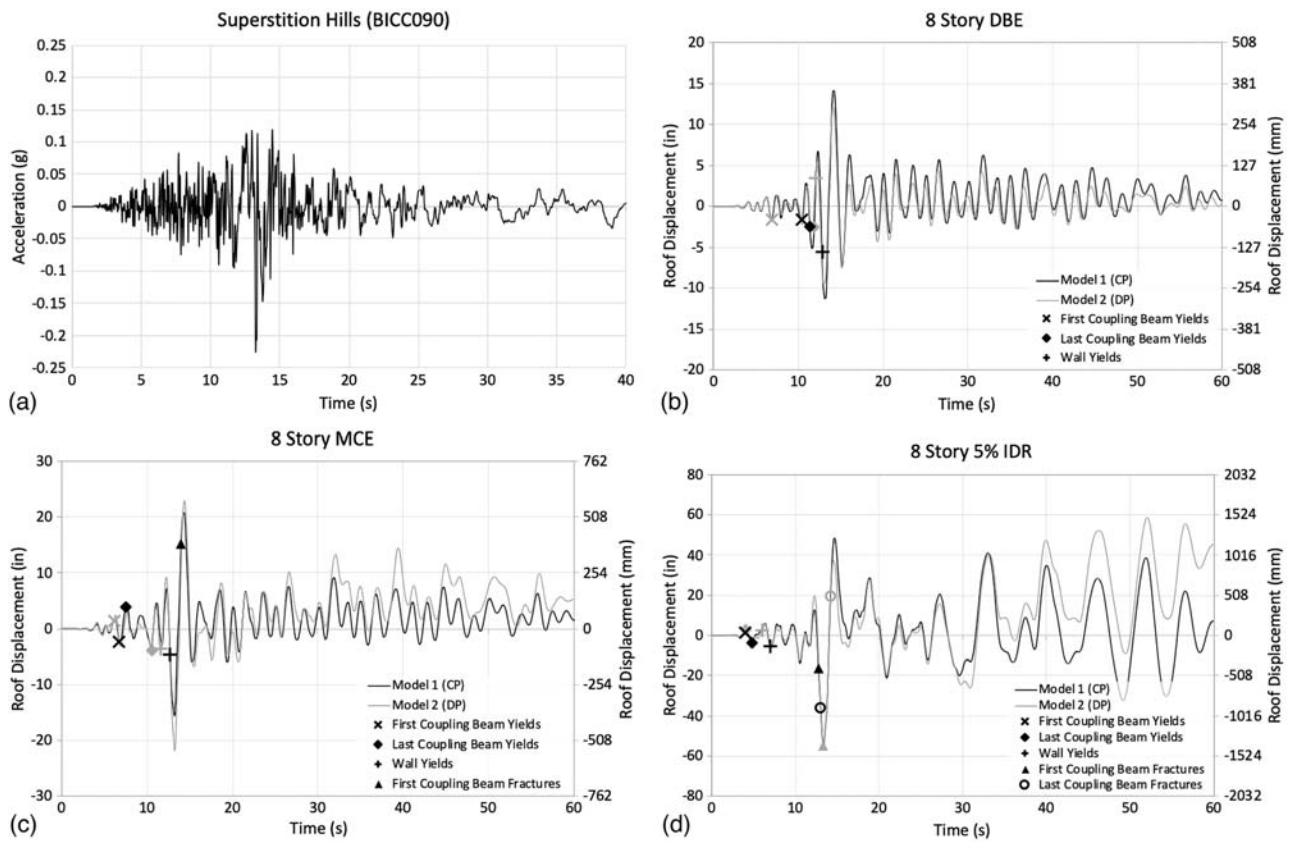


**Fig. 14.** (a) Superstition Hills acceleration versus time ground motion; (b) CP and DP model results for the 8-story structure subjected to the DBE; (c) CP and DP model results for the 8-story structure subjected to the MCE; and (d) CP and DP model results for the 8-story structure subjected to the FLE.

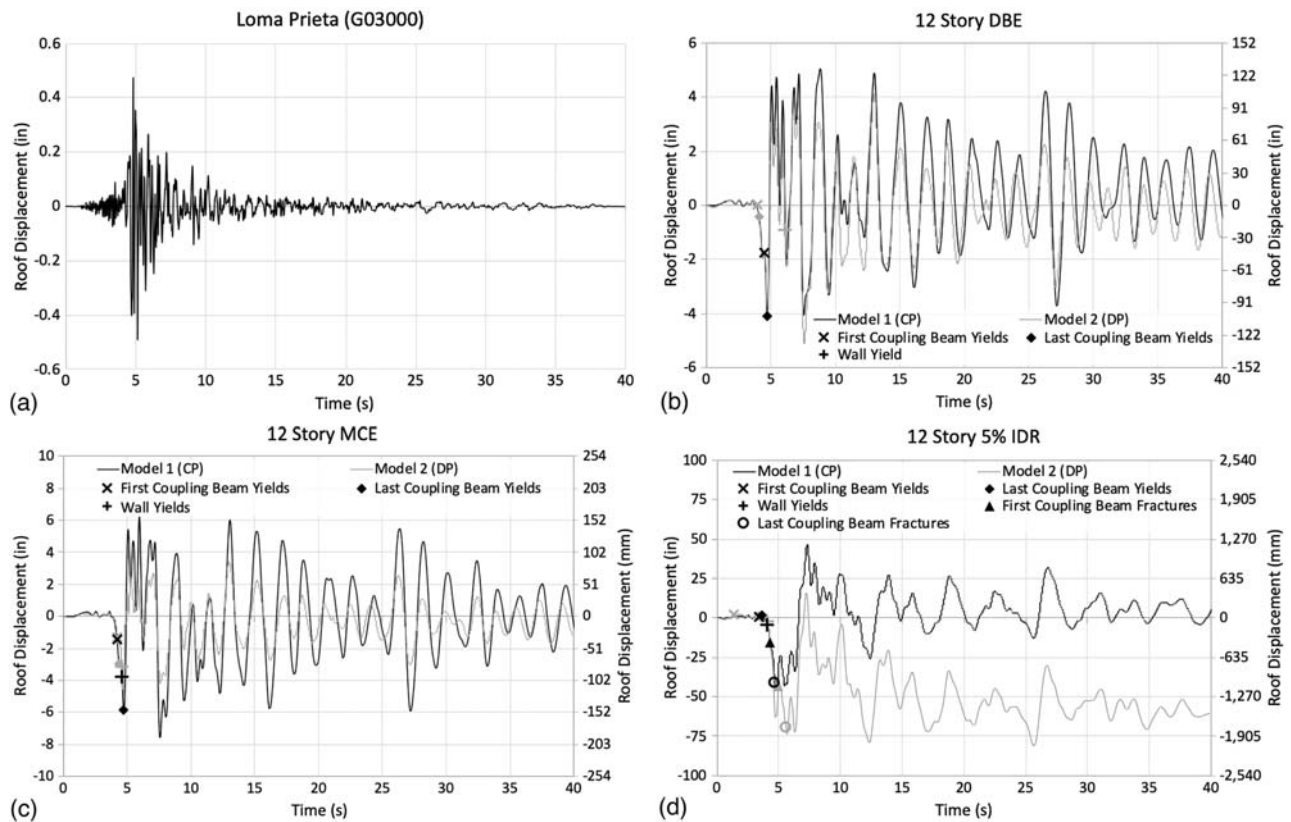


**Fig. 15.** (a) Loma Prieta acceleration versus time ground motion; (b) CP and DP model results for the 12-story structure subjected to the DBE; (c) CP and DP model results for the 12-story structure subjected to the MCE; and (d) CP and DP model results for the 12-story structure subjected to the FLE.

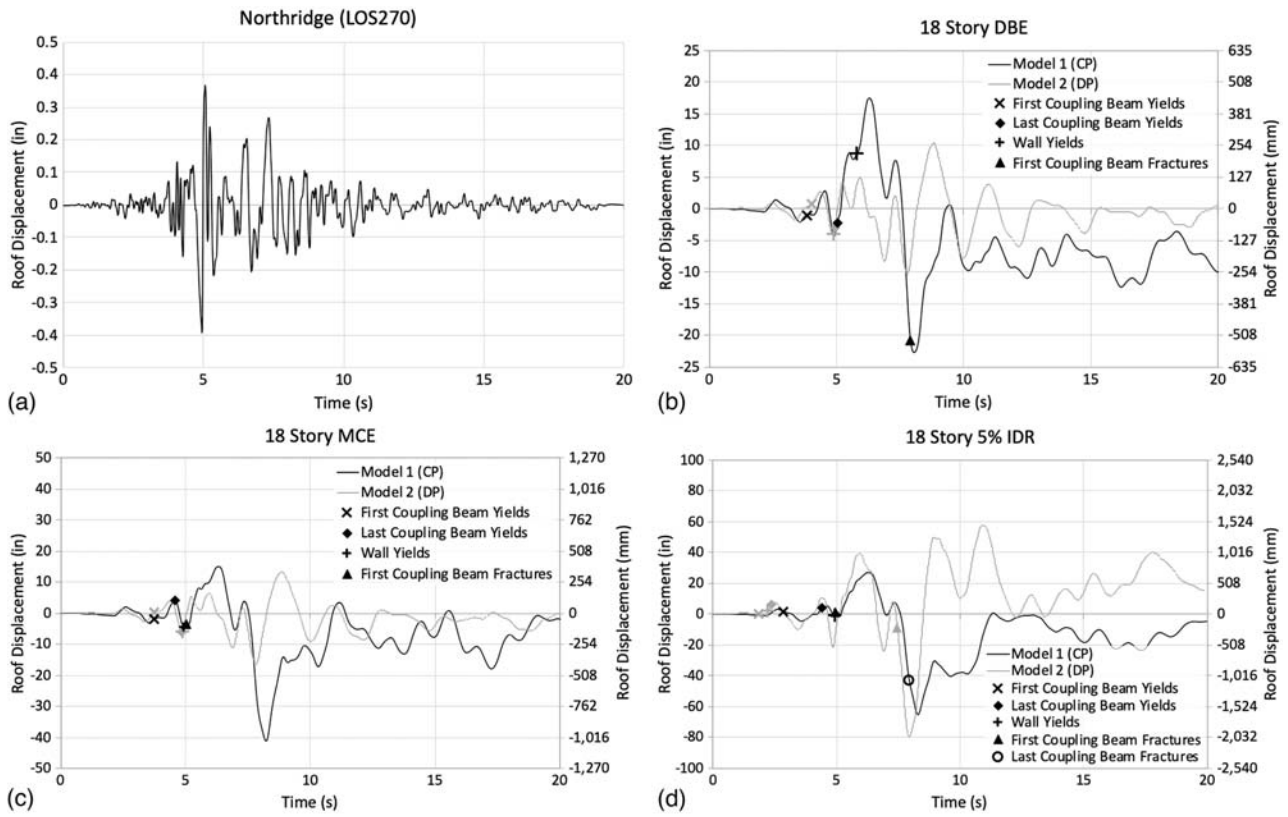


**Fig. 16.** (a) Northridge acceleration versus time ground motion; (b) CP and DP model results for the 18-story structure subjected to CP and DP model results for the 18-story structure subjected to the DBE; (c) CP and DP model results for the 18-story structure subjected to the MCE; and (d) CP and DP model results for the 18-story structure subjected to the FLE.

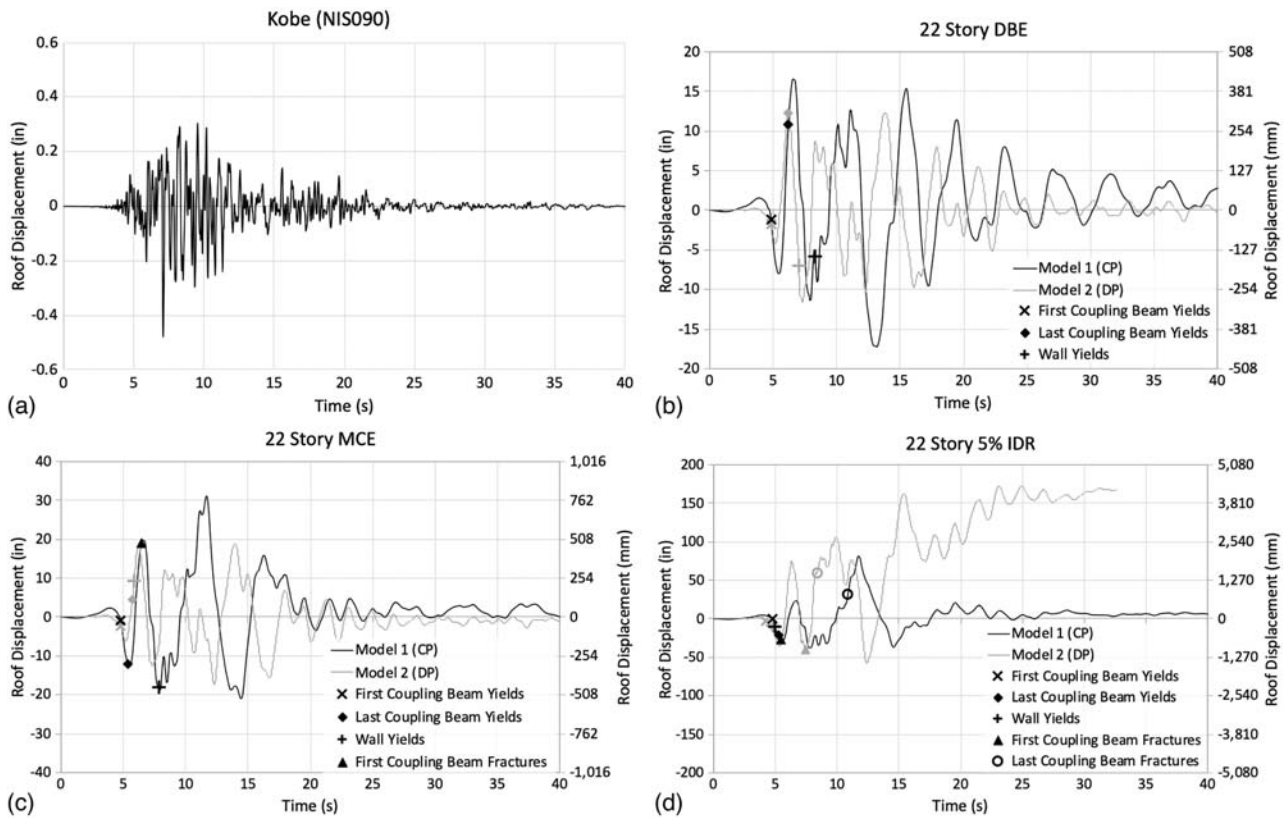


**Fig. 17.** (a) Kobe acceleration versus time ground motion; (b) CP and DP model results for 22-story structure subjected to the DBE; (c) CP and DP model results for 22-story structure subjected to the MCE; and (d) CP and DP model results for 22-story structure subjected to the FLE.

of the milestones (first coupling beam yielding, final coupling beam yielding, wall yielding, first coupling beam fractures, and final coupling beam fractures) are discussed here for these example structures. Of all the analyses, the MCE response for the 18-story structure, and the MCE and FLE responses for the 22-story structure deviated slightly from the expected progression of milestones.

For the CP model, the 18-story MCE response [Fig. 16(c)] showed wall yielding preceding yielding in all coupling beams. Although the difference is observable on the plot due to the sharp increase in roof displacement between these two events, the time between the two events was a fraction of a second. Moreover, the DBE and FLE responses exhibited the expected progression of milestone. Therefore, this variation from the anticipated failure mechanism is considered to be marginal. Nevertheless, as the height of the building increases, the milestone corresponding to initiation of yielding at the base of the wall may occur after formation of most plastic hinges in the coupling beams along the height of the structure, but not necessarily before the formation of plastic hinges in all coupling beams along this height. The reasons for this change in progression are described subsequently.

For the 22-story structure subjected to the MCE, coupling beam fracture occurred before all coupling beams yielded [Fig. 17(c)] in the CP model. This behavior occurred because of the conservative concentrated plasticity hinge model (with rotation capacity of 0.03 rad at fracture) for all the coupling beams, further exacerbated by higher-mode effects associated with the 22-story structure. The assumption that all coupling beams along the height of the structure engage equally and form plastic hinges at the ends becomes invalid when the rotational demand on the critical coupling beam (i.e., the first coupling beam to yield) exceeds the plastic rotation capacity (0.03 rad) before hinging of all other coupling beams. Simply put, the plastic rotation capacity of the coupling beams is finite, and as the height (and the number of coupling beams) of the structure increases, at some point the critical coupling beams do not have enough ductility for all other coupling beams to hinge before the initiation of fracture in the critical coupling beam. For the 22-story structure subjected to the FLE [Fig. 17(d)] in the CP model, the 22-story structure experienced wall yielding slightly before yielding of all the coupling beams. However, the first four milestones for this record occurred within less than 1 s. The wall yielding and yielding of all coupling beam occurred less than 0.25 s apart. This variation from the anticipated failure sequence is considered to be marginal.

For the DP models, responses followed the expected progression of milestones and confirm that the nonlinear dynamic responses generally were in accordance with the capacity design principle. Differences in the time-history response between the two models became more accentuated for the taller buildings, which is logical given that the models largely differed in how the coupling beams were modeled (i.e., the more stories, the larger was the number of coupling beams, and the greater was the divergence). In addition, after the last coupling beam fractured, the DP model indicated more displacement and permanent deformation than that in the CP model. Despite these differences, both models (CP and DP) showed that the structures could develop the maximum interstory drift ratio of 5% for the FLE without collapse.

## Conclusions

CC-PSW/CF systems have emerged as a viable seismic force resisting system for tall building construction. The capacity design procedure outlined in this paper is consistent with the philosophy adopted for other steel seismic force resisting systems included in

AISC 341-16 (AISC 2016a). The capacity design philosophy for CC-PSW/CF system relies on a strong wall–weak coupling beam approach in which wall elements are sized to resist the capacity limited loads from coupling beam elements.

Nonlinear push-over analyses and time-history analyses of CC-PSW/CFs, using three different modeling approaches, consistently showed a progression of milestones that met the intent of the capacity design philosophy. The preferred sequence of yielding in coupling beams along the structure height, yielding in walls at the base, fracture in coupling beams, and fracture in walls generally was observed in a range of example structures considered, with progressively more of these events happening up to the failure-level earthquakes. These failure-level earthquakes, which are significantly more severe than the design basis or maximum considered earthquakes, were defined here as those resulting in maximum interstory drifts of 5% for the selected ground motions considered, which conservatively was assumed to be failure for the purpose of these evaluations. This performance confirms that the capacity design philosophy presented in this paper can lead to overall structure or system design exhibiting a desirable ductile seismic performance. As the structure height increases beyond the permitted value 64 m (210 ft), yielding (not plastic hinging) may occur at the base of the C-PSW/CF walls before the formation of plastic hinges in all coupling beams along the height of the structure. This does not hamper the overall seismic performance or ductility of the system.

## Data Availability Statement

Some or all data, models, or code that support the findings of this study are available from the corresponding author upon reasonable request.

## Acknowledgments

The project was supported by the Charles Pankow Foundation and the American Institute of Steel Construction, through CPF research Grant #05-17 awarded to Michel Bruneau from the University at Buffalo and Amit H. Varma from Purdue University. All opinions, findings, conclusions, and recommendations presented in this paper are those of the authors and do not necessarily reflect the view of the sponsors. The researchers are grateful to members of the FEMA P695 peer review panel (Gregory G. Deierlein, Professor, Stanford University; Ron Klemencic, Chairman and CEO, Magnusson Klemencic and Associates; and Rafael Sabelli, Principal and Director of Seismic Design, Walter P. Moore), and members of the project advisory team (Larry Kruth, Vice President, AISC; John D. Hooper, Senior Principal/Director of Earthquake Engineering, MKA; Jim Malley, Senior Principal, Degenkolb Engineers; Bonnie Manley, Regional Director of Construction Codes and Standards, American Iron and Steel Institute; and Tom Sabol, Principal, Englekirk Institution) for their technical guidance.

## References

- About Rainier Square. n.d. "Rainier square." Accessed July 1, 2021. <https://www.rainiersquare.com/about/>.
- Agrawal, S., M. Broberg, and A. H. Varma. 2020. *Seismic design coefficients for SpeedCore or composite plate shear walls—Concrete filled (C-PSW/CF)*. Bowen Laboratory Research Reports. Paper 1. West Lafayette, IN: Lyles School of Civil Engineering, Purdue Univ.

- AISC. 2016a. *Seismic provisions for structural steel buildings*. ANSI/AISC 341-16. Chicago: AISC.
- AISC. 2016b. *Specification for structural steel buildings*. ANSI/AISC 360-22. Chicago: AISC.
- AISC. 2018. *Specification for safety-related steel structures for nuclear facilities*. ANSI/AISC N690-18. Chicago: AISC.
- AISC. 2022a. *Seismic provisions for structural steel buildings: Public review ballot*. ANSI/AISC 341-22. Chicago: AISC.
- AISC. 2022b. *Specification for structural steel buildings: Public review ballot*. ANSI/AISC 360-22. Chicago: AISC.
- Alzeni, Y., and M. Bruneau. 2017. "In-plane cyclic testing of concrete filled sandwich steel panel walls with and without boundary elements." *J. Struct. Eng.* 143 (9): 04017115. [https://doi.org/10.1061/\(ASCE\)ST.1943-541X.0001791](https://doi.org/10.1061/(ASCE)ST.1943-541X.0001791).
- ASCE. 2017. *Seismic rehabilitation of existing buildings*. ASCE/SEI 41-17. Reston, VA: ASCE.
- ASCE. 2022. *Minimum design loads for buildings and other structures: Public review ballot*. ASCE 7. Reston, VA: ASCE.
- Booth, P. N., S. R. Bhardwaj, T.-C. Tseng, J. Seo, and A. H. Varma. 2020. "Ultimate shear strength of steel-plate composite (SC) walls with boundary elements." *J. Constr. Steel Res.* 165 (Feb): 105810. <https://doi.org/10.1016/j.jcsr.2019.105810>.
- Bruneau, M., C. Uang, and A. Whittaker. 2011. *Ductile design of steel structures*. 2nd ed. New York: McGraw-Hill.
- Bruneau, M., A. H. Varma, E. Kizilarlan, M. Broberg, S. Shafaei, and J. Seo. 2019. *R-factors for coupled composite plate shear walls—Concrete filled (coupled-C-PSW/CF)*. Final Project Report, Charles Pankow Foundation, CPF #06-16. McLean, VA: Charles Pankow Foundation.
- FEMA. 2020. *NEHRP recommended seismic provisions for new buildings and other structures. Volume 1: Part 1 provisions, part 2 commentary*. FEMA P-2082-1. Washington, DC: Building Seismic Safety Council, National Institute of Building Sciences.
- Home. n.d. "200 Park Avenue San Jose." Accessed July 1, 2021. <https://200parkavesanjose.com/>.
- ICBO (International Conference of Building Officials). 1985. *Uniform building code*. Whittier, CA: ICBO.
- Kenarangi, H., M. Bruneau, A. Varma, and M. Ahmad. 2021a. "Simplified equations for shear strength of composite concrete filled steel tubes." *Eng. J.* 58 (3): 197–221.
- Kenarangi, H., E. Kizilarlan, and M. Bruneau. 2021b. "Cyclic behavior of C-shaped composite plate shear walls—Concrete filled." *Eng. Struct. J.* 226 (1): 111306. <https://doi.org/10.1016/j.engstruct.2020.111306>.
- Kizilarlan, E., M. Broberg, S. Shafaei, A. H. Varma, and M. Bruneau. 2021a. "Non-linear analysis models for composite plate shear walls—concrete filled (C-PSW/CF)." *J. Constr. Steel Res.* 184 (Sep): 106803. <https://doi.org/10.1016/j.jcsr.2021.106803>.
- Kizilarlan, E., M. Broberg, S. Shafaei, A. H. Varma, and M. Bruneau. 2021b. "Seismic design coefficients and factors for coupled composite plate shear walls/ concrete filled (CC-PSW/CF)." *Eng. Struct.* 244 (Oct): 112766. <https://doi.org/10.1016/j.engstruct.2021.112766>.
- Kurt, E. G., A. H. Varma, P. Booth, and A. S. Whittaker. 2016. "In-plane behavior and design of rectangular SC wall piers without boundary elements." *J. Struct. Eng.* 142 (6): 04016026. [https://doi.org/10.1061/\(ASCE\)ST.1943-541X.0001481](https://doi.org/10.1061/(ASCE)ST.1943-541X.0001481).
- Morgen, B., R. Klemencic, and A. H. Varma. 2018. *Core solution—Modern steel construction*. Chicago: AISC.
- Nie, J.-G., H.-S. Hu, and M. R. Eatherton. 2014. "Concrete filled steel plate composite coupling beams: Experimental study." *J. Constr. Steel Res.* 94 (Mar): 49–63. <https://doi.org/10.1016/j.jcsr.2013.10.024>.
- Park, R., and T. Paulay. 1975. "Ductile reinforced concrete frames." *Bulletin of the New Zealand Society for Earthquake Engineering* 8 (1): 70–90.
- Post, N. M. 2020. "Rainier Square erector says speed core could rise even faster." Accessed March 4, 2020. [www.enr.com/articles/48817-rainier-square-erector-says-speed-core-could-rise-even-faster](http://www.enr.com/articles/48817-rainier-square-erector-says-speed-core-could-rise-even-faster).
- SEAOC (Structural Engineers Association of California). 1980. *Recommended lateral force requirements and commentary*. Sacramento, CA: SEAOC.
- Seo, J., A. H. Varma, K. Sener, and D. Ayhan. 2016. "Steel-plate composite (SC) walls: In-plane shear behavior, database, and design." *J. Constr. Steel Res.* 119 (Mar): 202–215. <https://doi.org/10.1016/j.jcsr.2015.12.013>.
- Shafaei, S. 2020. "Seismic and wind behavior of planar composite plate shear walls concrete filled (C-PSWCF)." Ph.D. dissertation, Lyles School of Civil Engineering, Purdue Univ.
- Shafaei, S., A. H. Varma, M. Broberg, and R. Klemencic. 2021a. "Modeling the cyclic behavior of composite plate shear walls/concrete filled (C-PSW/CF)." *J. Constr. Steel Res.* 184 (2021): 106810. <https://doi.org/10.1016/j.jcsr.2021.106810>.
- Shafaei, S., A. H. Varma, J. Seo, and R. Klemencic. 2021b. "Cyclic lateral loading behavior of composite plate shear walls/concrete filled." *J. Struct. Eng.* 147 (10): 04021145. [https://doi.org/10.1061/\(ASCE\)ST.1943-541X.0003091](https://doi.org/10.1061/(ASCE)ST.1943-541X.0003091).
- Tauberg, N., K. Kolozvari, and J. Wallace. 2019. *Ductile reinforced concrete coupled walls: FEMA P695 Study*. Final Project Report, Submitted to the Charles Pankow Foundation for CPF research grant #06-17. McLean, VA: Charles Pankow Foundation.
- Uang, C.-M., and M. Bruneau. 2018. "State-of-the-art on seismic design of steel structures." *J. Struct. Eng.* 144 (4): 03118002. [https://doi.org/10.1061/\(ASCE\)ST.1943-541X.0001973](https://doi.org/10.1061/(ASCE)ST.1943-541X.0001973).
- Varma, A. H., M. Ahmad, S. Shafaei, and T. Bradt. 2021. *Seismic design and behavior of composite coupling beam-to-C-PSW/CF connections*. Final Project Rep. for Research Grant #06-16. McLean, VA: Charles Pankow Foundation and American Institute of Steel Construction.
- Varma, A. H., M. Broberg, S. Shafaei, and A. A. Taghipour. 2022. *Design guide 37*. Chicago: AISC.
- Varma, A. H., S. Shafaei, and R. Klemencic. 2019. "Steel modules of composite plate shear walls: Behavior, stability and design." *Thin-Walled Struct.* 145 (Dec): 106384. <https://doi.org/10.1016/j.tws.2019.106384>.
- Varma, A. H., K. Zhang, H. Chi, P. N. Booth, and T. Baker. 2011. "In-plane shear behavior of SC composite walls: Theory vs. experiment." Accessed July 1, 2021. <http://engineering.purdue.edu/~ahvarma/Publications/p764.pdf>.
- Zhang, K., J. Seo, and A. H. Varma. 2020. "Steel-plate composite (SC) walls: Local buckling and design for axial compression." *J. Struct. Eng.* 146 (4): 04020044. [https://doi.org/10.1061/\(ASCE\)ST.1943-541X.0002545](https://doi.org/10.1061/(ASCE)ST.1943-541X.0002545).
- Zhang, K., A. H. Varma, S. R. Malushte, and S. Gallocher. 2014. "Effect of shear connectors on local buckling and composite action in steel concrete composite walls." *Nucl. Eng. Des.* 269 (Apr): 231–239. <https://doi.org/10.1016/j.nucengdes.2013.08.035>.